

X-ray Emission from Young Stellar Objects in the ϵ Chamaeleontis Group: the Herbig Ae Star HD 104237 and Associated Low-Mass Stars

Paola Testa^{1,2}, David P. Huenemoerder¹, Norbert S. Schulz¹, Kazunori Ishibashi^{1,3}

ABSTRACT

We present *Chandra*-HETGS observations of the Herbig Ae star HD 104237 and the associated young stars comprising lower mass stars, in the $0.15\text{-}1.75M_{\odot}$ mass range, in their pre-main sequence phase. The brightest X-ray source in the association is the central system harboring the Herbig Ae primary, and a K3 companion. Its X-ray variability indicates modulation possibly on time scales of the rotation period of the Herbig Ae star, and this would imply that the primary significantly contributes to the overall emission. The spectrum of the Herbig Ae+K3 system shows a soft component significantly more pronounced than in other K-type young stars. This soft emission is reminiscent of the unusually soft spectra observed for the single Herbig Ae stars HD 163296 and AB Aur, and therefore we tentatively attribute it to the Herbig Ae of the binary system. The HETGS spectrum shows strong emission lines corresponding to a wide range of plasma temperatures. The He-like triplet of Mg XI and Ne IX suggest the presence of plasma at densities of about 10^{12} cm^{-3} , possibly indicating accretion related X-ray production mechanism.

The analysis of the zero-order spectra of the other sources indicates X-ray emission characteristics typical of pre-main sequence stars of similar spectral type, with the exception of the T Tauri HD 104237-D, whose extremely soft emission is very similar to the emission of the classical T Tauri star TW Hya, and suggests X-ray production by shocked accreting plasma.

Subject headings: X-rays: stars — stars: late-type — stars: individual: HD 104237

¹Massachusetts Institute of Technology, Kavli Institute for Astrophysics and Space Research, 70 Vassar street, Cambridge, MA 02139, USA; testa@space.mit.edu

²Current address: Smithsonian Astrophysical Observatory, 60 Garden street, MS 58, Cambridge, MA 02138, USA; ptesta@cfa.harvard.edu

³NorthWest Research Associates Inc., 3380 Mitchell Lane, Boulder, CO 80301, USA

1. Introduction

Nearby young associations provide ideal targets for the study of star and planet formation, and have sparked growing interest in the past few years. The early evolution of young stars is strongly dependent on stellar mass (e.g., Larson 1972). For low-mass stars ($M_\star \lesssim 2M_\odot$) the accretion timescales are shorter than the evolution time to the zero-age main sequence, and these stars can be observed in their pre-main sequence (PMS) T Tauri phase (D’Antona & Mazzitelli 1994). In massive protostars ($M_\star \gtrsim 10M_\odot$), however, core hydrogen burning already starts during the accretion phase (Appenzeller 1994; Bernasconi & Maeder 1996). The behavior at the boundaries between high and low mass ranges is yet unclear (Palla & Stahler 1993).

Herbig Ae stars (HAe; Herbig 1960) are PMS stars of intermediate mass ($\sim 2\text{--}10M_\odot$), and share several characteristics with T Tauri stars (TTS), such as IR excess emission, irregular photometric variability, and disk properties (Waters & Waelkens 1998; Mannings & Sargent 1997). HAe stars show evidence for a disk-like geometry of the circumstellar material, and the disk properties are similar to those of TTS (Mannings & Sargent 1997; Grady et al. 1999). There is some evidence of magnetic accretion in HAe stars, analogous to the magnetospheric accretion scenario generally accepted for classical TTS (CTTS, i.e. TTS that are still actively accreting) and are therefore thought to be more massive analogs of CTTS (e.g., Muzerolle et al. 2004; Grady et al. 2004; Guimarães et al. 2006). While magnetic fields have been detected in a few HAe stars (e.g., Donati et al. 1997; Hubrig et al. 2004), their origins are still unknown; however, a shear magnetic model does allow generation of magnetic fields in the early evolutionary stages of A-stars (Tout & Pringle 1995).

Systematic X-ray studies have shown that HAe stars are moderately bright X-ray sources (Damiani et al. 1994; Zinnecker & Preibisch 1994; Hamaguchi et al. 2005; Stelzer et al. 2006). Since main sequence A-stars are not known to be luminous X-ray sources due to lack of strong enough winds or magnetic-dynamo driven coronae, the findings may imply that the physical characteristics of young A-stars differ from those of main sequence A-stars.

HAe X-ray emission mechanisms remain unknown. Early studies based on ROSAT and *Einstein* observations proposed the standard wind shock model as for early-type massive stars (Damiani et al. 1994; Zinnecker & Preibisch 1994). However, typical L_X/L_{bol} ratios found for HAe stars are significantly higher than the empirical luminosity ratio of 10^{-7} for early type stars (Skinner et al. 2004), casting some doubt for this paradigm. Also, the high X-ray temperature ($> 10^7$ K) component found for a large fraction of HAe X-ray sources (see e.g., Skinner et al. 2004; Hamaguchi et al. 2005; Stelzer et al. 2006) cannot be produced through this mechanism. Others works attribute the emission to magnetic activity (either coronal activity as in late-type stars, or magnetic activity due to star-disk interaction),

or to unresolved late-type companions (Hamaguchi et al. 2005; Skinner & Yamauchi 1996; Skinner et al. 2004; Stelzer et al. 2006).

Another emission mechanism possibly at work in HAe stars is X-ray emission from shocks in accreting plasma, proposed as the production mechanism for soft X-rays in several CTTS (TW Hya, BP Tau, V4046 Sgr, MP Mus; Kastner et al. 2002; Stelzer & Schmitt 2004; Schmitt et al. 2005; Günther et al. 2006; Argiroffi et al. 2007). For these CTTS, *Chandra* and XMM-*Newton* high resolution spectra have revealed peculiar characteristics with respect to all other observed stellar spectra, in particular showing (i) soft excess—prominent cool component at temperatures of $\sim 3 \times 10^6$ K, TW Hya being an extreme case, where this soft component largely dominates the X-ray spectrum; (ii) unusually high density ($n_e \gtrsim 10^{12} \text{ cm}^{-3}$) for the cool ($T \sim 2 - 4 \times 10^6$ K) plasma, as diagnosed through the analysis of the He-like triplets line ratios; (iii) peculiar abundances—extremely high Ne, low metal abundances (Kastner et al. 2002; Stelzer & Schmitt 2004; Drake et al. 2005). Analogously, *Chandra* imaging spectra of the HAe star HD 163296 revealed a very soft spectrum (~ 0.5 keV) possibly suggesting accretion dominated X-ray emission (Swartz et al. 2005), as for the CTTS TW Hya (Kastner et al. 2002); Grady et al. (2007) also find extremely soft X-ray emission (~ 0.25 keV) from the Herbig Ae star HD 169142. Recently, XMM-*Newton* observations of the HAe star AB Aur have shown a very similar soft spectrum (Telleschi et al. 2007). In this case, the high resolution spectrum provides additional diagnostics: the high forbidden/intercombination ratios (f/i) of the He-like triplets, especially O VII, indicate the absence of high density and high UV field, expected if X-rays are produced in the accretion shocks, and rule out accretion-related X-ray emission for AB Aur. For AB Aur, which has spectral type A0, the photospheric UV emission is strong enough to alter the O He-like triplet up to several stellar radii from the surface; the large measured O VII f/i line ratio, constrains the emission to originate high above the photosphere ($\gtrsim 3R_*$) and therefore it implies that also coronal emission is unlikely for AB Aur. A plausible alternative for this source is X-ray emission from magnetically confined winds, as in the scenario of Babel & Montmerle (1997). It is important to keep in mind that some of the different X-ray emission mechanisms might not be mutually exclusive and instead they might coexist, as seems to be the case for some CTTS (Schmitt et al. 2005; Günther et al. 2006; Argiroffi et al. 2007) where both magnetically confined coronal plasma and accretion streams likely contributes to the overall X-ray emission.

HD 104237 is one of the nearest known ($d = 116$ pc; Perryman et al. 1997) and well studied HAe stars, and it is also a strong X-ray source ($L_X \sim 2 \times 10^{30} \text{ erg s}^{-1}$). *Chandra* observations have spatially resolved the X-ray emission from HD 104237, showing that the brightest X-ray source is coincident with the HAe source, and identifying 4 previously unknown nearby sources, likely TTS forming a young stellar group associated with HD 104237 (Feigelson et al.

2003, hereafter FLG03; see §2). *Chandra* (FLG03) and *XMM-Newton* (Skinner et al. 2004) imaging spectra of this HAe star have shown the presence of hot plasma ($\gtrsim 2$ keV), taken as evidence of magnetic activity. HD 104237 with its proximity, high L_X , and low line-of-sight extinction is a unique target to study the X-ray emission mechanism in HAe stars, through high resolution spectroscopy. High resolution spectra provide plasma diagnostics which are the only means for detailed study of the physical conditions of the emitting material. Cool, dense plasma ($\log T[\text{K}] \sim 6.5$, $\log n_e[\text{cm}^{-3}] > 12$) is now thought to be a signature of accretion, while variable hot emission is indicative of magnetic activity.

In this paper we present *Chandra*-HETGS observations of HD 104237. The relatively long exposure of ~ 145 ks provides detailed information on the X-ray variability of the HAe star, as well as of other stars in the field, and it yielded a well exposed HETGS spectrum of the HAe star providing detailed diagnostics for the emitting plasma.

We present the characteristics of the targets in §2. The observations and our techniques of line flux measurement and spectral analysis are briefly described in §3. The results are presented in §4. We discuss the results and draw our conclusions in §5, and 6.

2. HD 104237: the Herbig Ae star and the T Tauri association

HD 104237 is the optically brightest HAe star, and it is also a moderately strong X-ray source with $\log L_X \sim 30.5$ erg/s, observed with ROSAT (Alcala et al. 1995), ASCA (Skinner & Yamauchi 1996), *Chandra* (FLG03), and *XMM-Newton* (Skinner et al. 2004).

Chandra imaging observations, thanks to the unprecedented sub-arcsecond spatial resolution, have revealed the presence of four other X-ray emitting young stellar objects associated with HD 104237, labeled B–E, A being the HAe star (Figure 1; see also FLG03). Grady et al. (2004) (hereafter G04) have conducted intensive high angular resolution multiwavelength imaging (optical, NIR, mid-IR), and spatially resolved spectroscopy (optical, UV, FUV) to probe the characteristics of A, and the associated star-forming environment. The comprehensive study by G04, has provided detailed information on the HAe star and constraints on possible close companions.

The stellar parameters of the members of this young (~ 2 -5 Myr) stellar group are listed in Table 1. IR excess, H α emission, and Li absorption indicate a T Tauri nature for the components B, D, and E (FLG03; G04). FLG03 hypothesized that C is a late M-type TTS or a brown dwarf.

HD 104237-A: HD 104237-A has been identified as an Herbig Ae star by Hu et al. (1989), based on its optical spectrum and IR excess. It was initially assigned a spectral type A0pe by

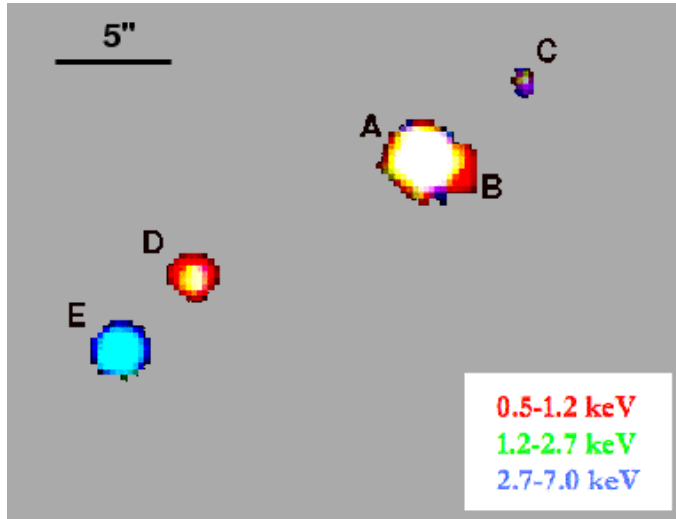


Fig. 1.— Color coded *Chandra* image of the HD 104237 field from our ~ 145 ks HETGS observation. The X-ray sources of the young stellar group are labeled following Feigelson et al. (FLG03). The separation between sources is listed in Table 1; all sources are within $\sim 20''$.

Walker & Wolstencroft (1988), then A4 ve by Hu et al. (1991), and recently G04 have revised its classification as A7.5 ve–A8 ve. The HAe star presents evidence of activity—as indicated by line emission, UV excess, outflows—and is still accreting at an estimated rate of $\sim 10^{-8} M_{\odot}/\text{yr}$ (G04, Garcia Lopez et al. 2006). UV high resolution spectra show P Cygni profiles for several lines (Blondel & Djie 2006). G04 also found a bipolar microjet and Herbig-Haro knots; from the analysis of proper motion of a knot they derived the inclination of the system to be $18^{\circ}_{-11}^{+14}$. The inclination may be a meaningful parameter for the detection of accretion signatures, assuming the geometry of magnetospheric accretion models; for instance, the CTTS TW Hydrae and BP Tau, whose soft X-ray emission appears accretion dominated, have both nearly pole-on aspects of 10° and 30° respectively. The observations suggest a magnetospheric accretion scenario for HD 104237-A similar to CTTS (G04). A magnetic field of this HAe has been marginally detected (~ 50 G; Donati et al. 1997). If the geometry of the accretion is similar in HD 104237-A we will likely observe almost along the accretion stream. The HD 104237-A disk extends at most to $0.6''$ (~ 70 AU).

HST observations put tight constraints on the distance of any unknown close companion to A (other than the resolved X-ray source B at $\sim 1.4''$ separation; G04), excluding the presence of a companion with distance r to the A star $0.05'' < r < 1''$, implying that a possible companion would have to be closer than ~ 5 AU to A. Böhm et al. (2004) through high resolution spectral observations (aimed at the study of δ Scuti pulsation observed for this

H Ae star) revealed the presence of a spectroscopic binary companion to the H Ae star, and determined the orbital parameters. They find a mass ratio $M_{\text{primary}}/M_{\text{secondary}} = 1.29 \pm 0.02$, and an orbital period of about 20 days, implying an average separation of ~ 0.15 AU. They assign a spectral type K3 to this spectroscopic companion which is responsible for the Li-line traces in the spectrum of the H Ae star revealed by FLG03 and which they attributed to contamination from the adjacent B component. The parameters of the H Ae star and the K3 close companion are included in Table 2. Recently, Tatulli et al. (2007) using near-IR interferometric observations of this H Ae star modeled the spatial distribution of the circumstellar material and outflows on AU scales; their observations are compatible with outflowing wind launched in the vicinity of the dusty disk inner rim ($\sim 0.2 - 0.5$ AU). Considering the very small distance between the spectroscopic binary components, the circumstellar disk of the H Ae star is likely a circumbinary disk, and this could in principle affect the magnetospheric accretion scenario and other phenomena occurring on small scales close to the stars.

The presence of this later type companion, unresolved in the X-ray observations, significantly changes the perspective for interpretation of the X-ray emission of HD 104237-A, as K-type PMS stars are known strong X-ray emitters (e.g., Getman et al. 2005). We will thoroughly discuss this issue in §5.

HD 104237-B: The proximity of HD 104237-B to the H Ae star hampers the precise determination of its stellar parameters, as thoroughly discussed by G04. FLG03 tentatively assigned a K spectral type to B due to the presence of Li-line features in the optical spectrum of HD 104237-A; however, these features are actually produced by the the K-type close companion subsequently discovered as discussed above. G04 finds that HD 104237-B is likely a M-type TTS on the basis of its infrared excess, and of its PSF in HST/STIS images, compatible with M3-M4 spectral type.

HD 104237-C: FLG03 has tentatively classified HD 104237-C as a brown dwarf candidate.

HD 104237-D: The $H\alpha$ equivalent width, close to the classical TTS limit, the Li features, and the X-ray luminosity indicate the T Tauri nature of HD 104237-D (G04).

HD 104237-E: This star has a late spectral type, broad $H\alpha$ emission, and photometric variability, which are typical of accreting CTTS (G04). This source was also variable in X-rays and showed a remarkable change in emission level by a factor ~ 8 between the two short ACIS-I observations of FLG03, who also found it to be much more absorbed than the other stars in the association. This suggests that the obscuration is due to local circumstellar material.

3. Observations and Analysis

We observed the Herbig Ae star HD 104237 and the group of young stellar objects associated to it with the *Chandra* High Energy Transmission Grating Spectrometer (see Canizares et al. 2005 for a description of the instrumentation) for a total exposure time of 145 ks. The details of the observations are presented in Table 3.

We also re-analyzed the ACIS imaging-mode observations of FLG03 (ObsID 2404 and 3428).

The data used here have been reprocessed using standard CIAO (Fruscione et al. 2006) v3.4 tools. Effective areas were calculated using standard CIAO procedures, which include an appropriate observation-specific correction for the time-dependent ACIS contamination layer.

Spectral analysis of grating and zeroth order spectra were done with the Interactive Spectral Interpretation System (ISIS⁴) version 1.4.2 (Houck & Denicola 2000).

In Figure 1 we present a color coded image of the *Chandra*-HETGS observations where photons energies in the range 2.7 – 7.0 keV correspond to blue, 1.2 – 2.7 keV to green, and 0.5 – 1.2 keV to red. The X-ray sources are labeled following the classification of FLG03.

In the following section we present the analysis of the X-ray emission of all sources of this young stellar association. We analyzed the low resolution spectra and variability for all group members, and the high resolution spectrum of source A which has enough counts for a meaningful analysis of the dispersed photons.

4. Results

In the total ~ 145 ks HETG observations we detected all sources studied in FLG03. Source A is the strongest X-ray source but even for this source the pileup in the zeroth order is essentially negligible (up to a few %). Source E and D have comparable count rates about an order of magnitude smaller than for source A. Source B, which is at an angular distance of $\gtrsim 1''$ (FLG03, G04), is apparent as an elongation of source A in the SW direction; even though there is a small contamination of source B in the spectrum of source A its contribution to the A+B spectrum is lower than 10%. Finally, source C is detected at a 3σ level only for a portion of the observing time.

⁴ISIS is available at <http://space.mit.edu/cxc/isis/>

The HETG observations presented here provide significantly better statistics than the previous ACIS-I observations analyzed by FLG03. For source A, we obtained more than 3700 integrated zero-order counts vs. 640 of the short ACIS observations. For the sources B, C, D and E we obtain 152, 54, 251, and 543 zero-order counts which are a factor 2.5 to 9 times higher than the counts of the ACIS-I observations which were 44, 6, 70, 225, respectively.

In order to extract the zero-order spectrum of source B we needed to take into account the contamination of source A. This contamination was estimated by extracting the counts of source A in an annular region 2-4 pixels from the center, and excluding a sector containing source B (between -0.64 and 0.24 rad, where 0.0 is west and positive angles are in the north direction). These counts were then scaled to the region of extraction of source B and used as a background for this source.

4.1. Variability

All sources in the HD 104237 field appear to be variable. In Figure 2 we show the lightcurves obtained from zero-order photons for sources B, C, D, E. In order to show how significant the detection of source C is in the different segments of observation we also derived a lightcurve for the background, using an extraction region, close to source C, and with radius 4 times larger than the default value used for the extraction of the spectra of all sources, and then scaling the rate to the source region areas. All sources present significant variability over time scales of days to months.

In Figure 3 we plot the lightcurves of source A as obtained from the dispersed photons. In the upper panels we plot the lightcurve of all dispersed photons (black curves), and also the lightcurves in two spectral bands in order to show possible changes in spectral hardness: the hard band corresponding to the 1.5 – 8 keV energy range (blue curves), and the soft band corresponding to the 0.5 – 1.5 keV range (red curves). The lower panels show the corresponding hardness ratio (defined as [hard-soft]/[hard+soft]). These plots show that the source presents continuous variability (within a factor ~ 2 from an average value) on time scales from hours to days. However the observed variability does not show obvious similarities with very dynamic events such as flares, which are typical of active stellar coronae and are generally characterized by significant increases in hardness ratio and time scales of hours up to days for the most extreme events observed in very active young stars.

We searched for possible periodicity in the lightcurves of source A, in particular exploring possible periodic variation on the characteristic time scales of the system: the orbital period of the binary system ($P_{\text{orb}} = 19.859$ days; Böhm et al. 2004), and the rotation period. The

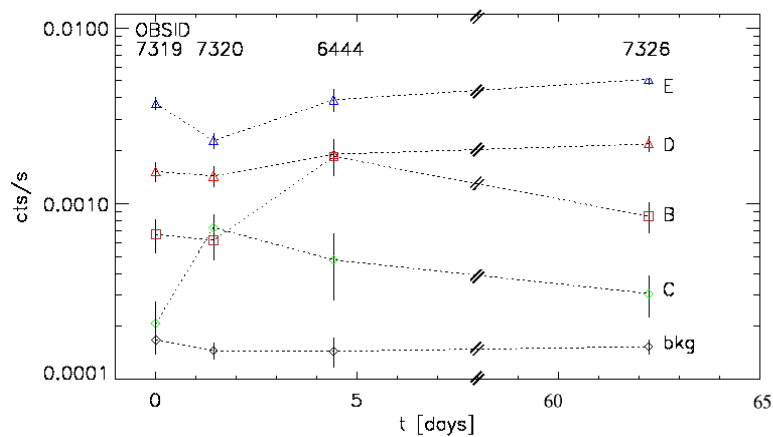


Fig. 2.— Zero order lightcurves of sources B, C, D, E, and for the background: we plot count rates with error bars for the four observations as a function of time; the last observation, carried out two months apart the first one is shifted by -50 days. The background rate was derived from a circular region close to source C, with a radius 4 times larger than the default extraction radius used for all the sources. The counts for source B are derived as described in the text with a procedure we devised to take into account and subtract the contamination of source A.

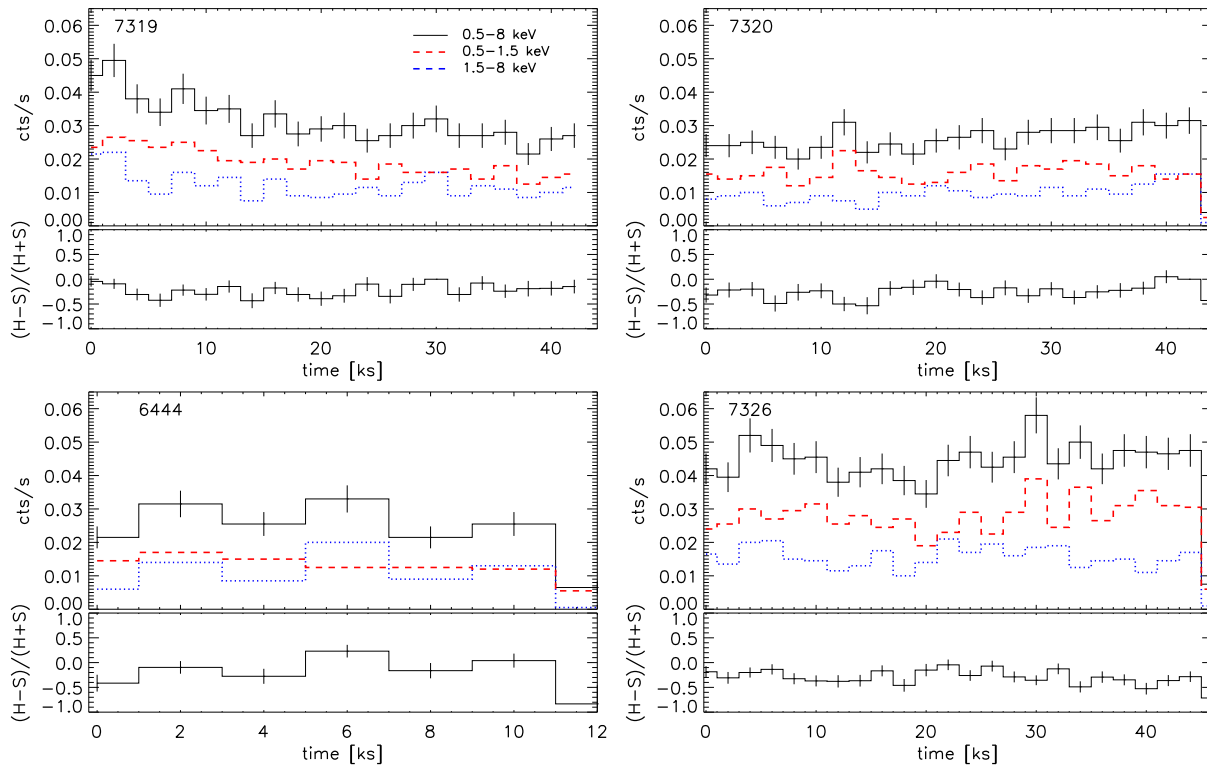


Fig. 3.— Lightcurves of first order dispersed photons of source A for each of the four observations, using a binsize of 2 ks. The upper panel of each plot shows the lightcurves of all the first order dispersed photons (solid line with error bars), and the lightcurves in two energy bands: a hard band (1.5 – 8 keV; dotted line) and a soft band (0.5 – 1.5 keV; dashed line). The lower panels show the corresponding hardness ratio defined as [hard-soft]/[hard+soft].

rotation period of this Herbig Ae star is however not well determined, therefore we used different estimates. Using the $v \sin i = 12 \text{ km s}^{-1}$ obtained by Donati et al. (1997) (derived from several photospheric spectral lines), the inclination $i = 18^\circ$ estimated by G04, and a stellar radius $R_\star = 2.5R_\odot$ (Böhm et al. 2006) we obtain a rotation period $P_{\text{rot}} = 3.26$ days; however, considering the uncertainties on all these parameters⁵, the rotation period is poorly determined. Böhm et al. (2006) present a possible indication of rotational modulation by studying modulation of lines forming close to the stellar photosphere: they find modulation in the H α line that might be due to rotation and it would yield $P_{\text{rot}} = 100 \pm 5$ hrs, i.e.

⁵For instance, Blondel & Djie (2006) assume very different values for both $v \sin i$ (150 km s⁻¹), and i (53°), which they infer from optical lines, and the redshifted component of the Ly α emission respectively.

$P_{\text{rot}} = 4.17 \pm 0.21$ days. Therefore we performed a period analysis in this range of periods and we find a best fit period of 95 hrs.

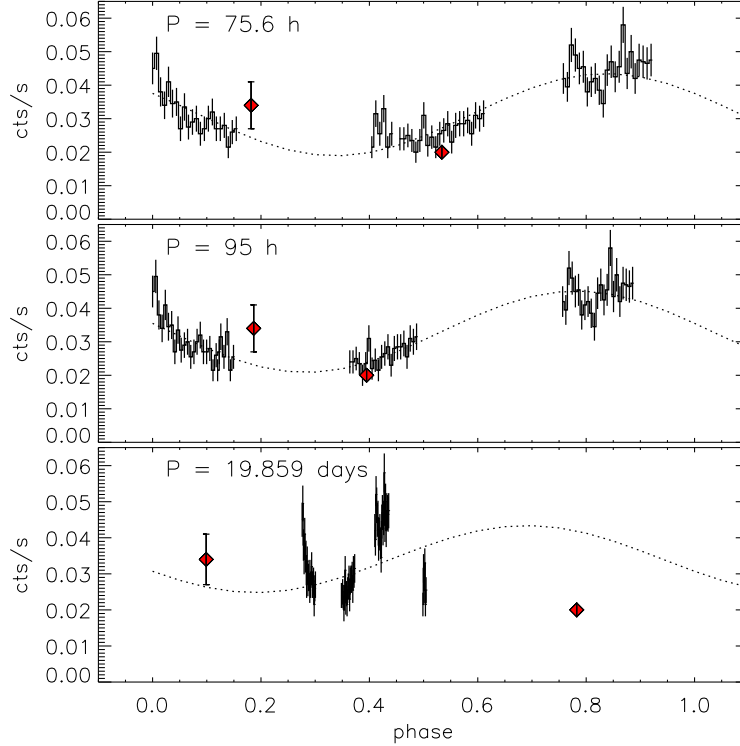


Fig. 4.— Lightcurves of dispersed photons of source A (binsize of 2 ks) phase-folded assuming three different periods: *top* – $P = 75.6$ h obtained assuming $v \sin i = 12 \text{ km s}^{-1}$ (Donati et al. 1997), $i = 18^\circ$ (G04), and $R_\star = 2.5R_\odot$ (Böhm et al. 2006); *middle* – $P = 95$ h (within range of possible rotational modulation observed in $H\alpha$ by Böhm et al. 2006; see text); *bottom* – $P = 19.859$ days = P_{orb} of the binary system of the Herbig Ae star HD 104237 + K3 companion (Böhm et al. 2004); phase 0 corresponds to the periastron passage. Filled symbols indicate the zero-order count rate predicted from modeling the ACIS-I observations (see text and Table 4). The dotted line represent a fit to the data with a simple sinusoidal curve plus a constant; while this function does not represent a specific physical model, the constant function can be interpreted as the emission level of the quiescent (i.e. more homogeneously distributed) corona, while the rotational modulation would be likely caused by the appearing and disappearing from view of compact regions of more intense X-ray emission.

Figure 4 shows the phase folded lightcurves for three different periods. All plots indicate that our X-ray observations do not provide a large phase coverage even for the shortest period, therefore making difficult to identify possible periodic modulation of the X-ray emission. Nevertheless, the observed lightcurve seem to be compatible with modulation on time scale

comparable with the rotation period as estimated by Böhm et al. (2006); if true this would imply that the Herbig Ae star is likely a significant contributor to the overall X-ray emission of the binary system. The variability does not show correlation with the orbital period of the HD 104237-A system of 19.859 days (bottom panel of Fig. 4).

In Figure 4 we also superimpose the count rates estimated for the two early ACIS-I observations studied by FLG03 (ObsID 2404 and 3428). FLG03 in their analysis assumed negligible N_{H} and did not account for pileup. In order to take into account these effects and estimate the expected count rate for these two observations, we re-analyzed the data using the pileup model of (Davis 2001) as implemented in ISIS. This model accounts for coincident detection of multiple photons and has the advantage of using all the counts in the source region, not just those in an outer, un-piled annulus. We found a two-temperature model was necessary, and that the pileup fraction was about 20%. In fitting the spectra we fixed the abundances to the values derived from the HETGS analysis, and the N_{H} to $2 \times 10^{21} \text{ cm}^{-2}$ (see detailed discussion in §4.2). We note that our analysis of the ACIS-I spectra of HD 104237-A yields for both temperature components lower values with respect to those found by FLG03; also, our derived luminosity values are larger than the values found by FLG03 (by about 20% and 50% respectively in the two observations). These discrepancies are due to the inclusion of interstellar absorption and pileup effects.

4.2. Low resolution spectra

The color coded image (Figure 1) shows that source E is characterized by a hard spectrum, source D is on the contrary extremely soft, and source A is an intermediate case. Here we present the low resolution spectra of source A, B, C, D, and E and the results of the fits to these spectra with isothermal or two-temperature plasma models.

For source A, the higher signal to noise allow us to study separately the low resolution spectra of each observation to highlight possible changes in the spectral characteristics with changes in the X-ray emission level. For all other sources due to the poorer statistics we combined the spectra of all four observations in order to improve the signal-to-noise ratio and better constrain the average spectral parameters.

We extracted the low resolution spectra of source A for each observation, and performed a fit with a thermal model of plasma in collisional ionization equilibrium with variable absorption. A single temperature model, even with variable abundances, does not provide a good fit to the spectrum. Therefore we use a 2-T component model with single N_{H} . The fits to the spectra obtained for the separate observations do not show significant changes in

the spectral parameters within the uncertainties, therefore we summed up the spectra for all four observations to better constrain the parameters of the model.

As thoroughly discussed in §4.3.1, the high-resolution spectrum provides additional strong constraints to the fit of the X-ray spectrum. Here we use the abundances found from the analysis of the dispersed spectra and we fit the low-resolutions spectrum with a 2-T model with abundances fixed to those values. This 2-T model, whose parameters are listed in Table 5, provides a good fit to the integrated zero-order spectrum of source A, and shown in Figure 5. We also fitted the model with a similar 2-T model but with variable abundances (model II in Table 5), however the comparison with model I indicates that this model does not provide a significantly better fit: when abundances are let free to vary their best fit values are very similar to the values found from the analysis of the dispersed spectra which provide more robust results because single lines are resolved and used for the determination of the element abundances (see §4.3.1).

Furthermore we explored two more different models: a 2-T model with fixed abundances as in I but different N_{H} for each temperature component (model III), and 3-T model with fixed abundances as in model I (model IV). The former model explores the scenario of two temperature components corresponding to different X-ray emitting plasma regions with different N_{H} , as likely for example if the two components are emitted by the two binary stars. Skinner & Yamauchi (1996) already investigated this possibility when analyzing the ASCA data and found a hot more absorbed component ($T \sim 20$ MK, $N_{\text{H}} \sim 1.7 \times 10^{22} \text{ cm}^{-3}$) and a cool slightly less absorbed component ($T \sim 2.5$ MK, $N_{\text{H}} \sim 6 \times 10^{21} \text{ cm}^{-3}$). They tentatively interpreted the hot absorbed component as produced by an embedded TTS companion, and the cool emission as the HAe star emission; the uncertainties however were too large to provide any real constraint to this model. From our data we find that the absorption of the hot component might be actually lower than the absorption of the cool component, but they are not significantly different within the uncertainties. The 3-T temperature best fit model has a cool component with parameters essentially identical to the 2-T models, while the hot component is redistributed in two hot components at 20 and 80 MK respectively; the only parameter slightly different is the lower absorption N_{H} . Neither of these two model provides a statistically better fit to the observed spectrum than the 2-T model with fixed abundances, therefore we consider model I (Table 5) the best fit to the low-resolution spectrum.

Comparing these results with the finding of analysis of previous X-ray observations of HD 104237 we note that the overall characteristics (T , L_{X}) of its X-ray emission seem remarkably constant for more than a decade, with $L_{\text{X}} \sim 2 \times 10^{30} \text{ erg s}^{-1}$ and at least two temperature components needed to explain its spectrum (Skinner & Yamauchi 1996, FLG03, Skinner et al. 2004; Stelzer et al. 2006). Both FLG03 and Stelzer et al. (2006) find

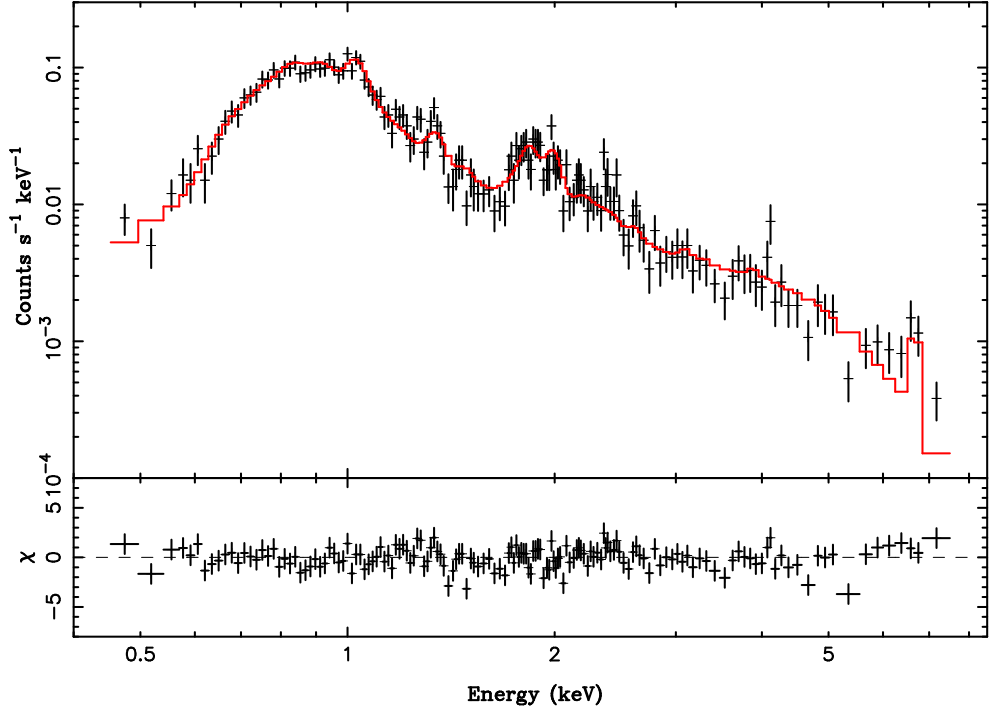


Fig. 5.— Zero order spectrum of HD 104237-A (data points) with best fit model superimposed (model I of Table 5; solid line). The best fit model is a two-temperature plasma model with $N_{\text{H}} = 1.7 \times 10^{21} \text{ cm}^{-2}$, $T_1 = 4.7 \times 10^6 \text{ K}$ (0.4 keV), $T_2 = 2.7 \times 10^7 \text{ K}$ (2.3 keV). The X-ray luminosity from this model is $2.9 \times 10^{30} \text{ erg s}^{-1}$ (corrected for absorption) in the 0.5-7 keV range.

from the analysis of *Chandra*-ACIS data slightly higher temperatures for both T components; however this can be explained considering that they assume essentially negligible N_{H} . Our model parameters compare well with the findings of Skinner et al. (2004) based on XMM-*Newton* data, the only significant difference being in the derived element abundances which Skinner et al. (2004) find to be significantly above solar for all elements except S, and Fe, about solar⁶.

The fits to the low resolution spectra of HD 104237-A all yield N_{H} values compatible with the visual extinction derived for this star: the N_{H} value spans the range 0.1-0.2 $\times 10^{22}$ cm⁻², which, using the conversion of Gorenstein (1975), corresponds to A_V in the range 0.45-0.9, in good agreement with values found from optical studies (e.g., 0.3 of van den Ancker et al. 1998, and 0.8 of Malfait et al. 1998). This is also consistent with previous findings of Skinner et al. (2004).

The zero-order spectra of the other four sources are shown in Figure 6 and 7, and the parameters of the fits with corresponding uncertainties are listed in Table 6.

The left panel of Figure 6 shows the zero-order spectrum of source B with the corresponding best fit model. We find that a model with a single temperature at ~ 1 keV and zero absorption reproduces well enough the observed spectrum. The parameters of the X-ray spectrum are rather typical of similar M-type TTS (see discussion in §5). However the relatively low number of counts (~ 150) obtained for this source does not allow to constrain the parameters very well, as demonstrated in the confidence contours in the N_{H} -T parameter space shown in the panel below the spectrum plot in Figure 6.

Source C is a very weak source for which very scarce information is available. On the basis of the X-ray observation and the (lack of) optical data, FLG03 proposed a possible identification as a brown dwarf; the association with the young stellar group of HD 104237 is uncertain. In our 145 ks observation we gathered about 54 net counts for source C (subtracting a background estimated on a nearby extraction region); the spectrum and the best fit model are shown in Figure 6. The poor statistics do not provide stringent constraints on the spectral properties of the X-ray emission of this source. Within the uncertainties, we find parameters compatible with the emission by a brown dwarf at the distance of HD 104237 confirming the findings of FLG03.

For source D, and E, which are identified as T Tauri stars associated to HD 104237, we

⁶They find Ne, Mg, Si, Ca, to be 2.3, 2, 2, 9.9 times solar respectively for their 2-T model, and 2.2, 1.7, 1.6, 6.6 times solar for their 3-T model. As discussed in §4.3.1 the analysis of the high resolution spectra allows to determine the element abundances accurately, ruling out such large values.

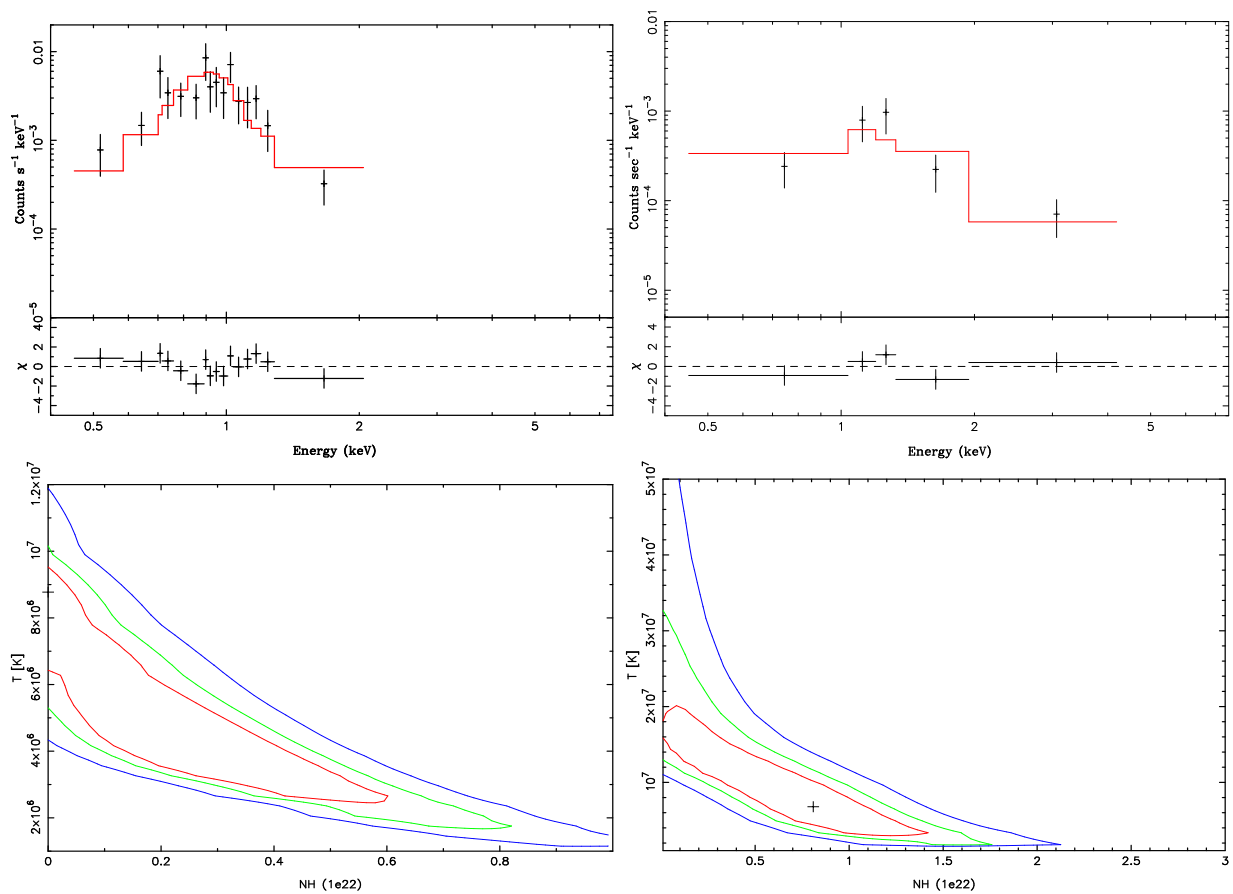


Fig. 6.— *Top*: Zero-order spectrum of HD 104237-B (*left*) and C (*right*), rebinned to a minimum 5 counts per bin, with corresponding best fit model. The parameters of the best fit models are listed in Table 6. *Bottom*: Confidence contours in the N_{H} - T space (68%, 90%, 98%) for source B (*left*) and C (*right*).

have obtained about 250 and 540 zero-order counts respectively, over the 145 ks observation. As already apparent in the color coded image (Fig. 1), source E is heavily absorbed and only the hard photons are detected. The spectral fit indicates in fact a large N_{H} of $3.4 \times 10^{22} \text{ cm}^{-2}$, much larger than the interstellar absorption and that can be therefore ascribed to local absorption from circumstellar material. This source is identified as a K3 classical T Tauri star, and the infrared excess detected by G04 provide further evidence of presence of large amounts of circumstellar material. Source D is a lower mass T Tauri star, of spectral-type M, border-line classical T Tauri star as indicated by the $H\alpha$ equivalent width very similar to source E (G04). At variance with respect to source E, infrared measurement do not indicate large infrared excess (G04; however the measurements are characterized by poorer statistics for this source and therefore the limits are not very stringent). Its X-ray spectrum is very soft for its emission level (its $L_{\text{X}} = 10^{30} \text{ erg s}^{-1}$ is rather large for M-type TTS; see §5 for a more detailed discussion), and it is fit well with an isothermal model with $T = 3 \times 10^6 \text{ K}$ (0.24 keV). These spectral parameters for source D, and E, are well determined within the statistical uncertainties as clear from the confidence contours in the N_{H} -T space shown in Figure 7 (bottom panels).

4.3. HETGS spectrum of HD 104237-A

A goal of our observing program was to obtain a high resolution X-ray spectrum of the Herbig Ae star with high signal-to-noise ratio, in order to investigate the X-ray production mechanisms in intermediate mass pre-main sequence stars. The HETGS spectrum of sources A and B cannot be resolved spatially in the dispersed spectra. However, our zero-order analysis (§4.2) indicates that component B's contribution is $\lesssim 10\%$ that of A. Henceforth we will refer to the spectrum as if from A alone, but it should be kept in mind that there is some level of contamination from B. Other sources in the field are distant enough that order-sorting results in unique determination in MEG-HEG crossed-order regions. In the 145 ks HETGS observation we obtained slightly more than 5000 total counts in the HEG and MEG -1,+1 orders.

In Figure 8 we show the high resolution spectrum of HD 104237-A, obtained by summing HEG and MEG spectra (-1 and +1 orders). The spectrum is dominated by line emission of H-like and He-like ions of Si, Mg, Ne, by Fe XVII transitions around 15\AA and 17\AA , and by transitions of H-like oxygen. Also, some continuum emission is present as well as transitions of highly ionized Fe around $\sim 11 \text{\AA}$ both indicating the presence of significant amounts of hot ($T \gtrsim 2 \times 10^7 \text{ K}$) plasma.

The measured line fluxes together with the statistical errors, are listed in Table 7.

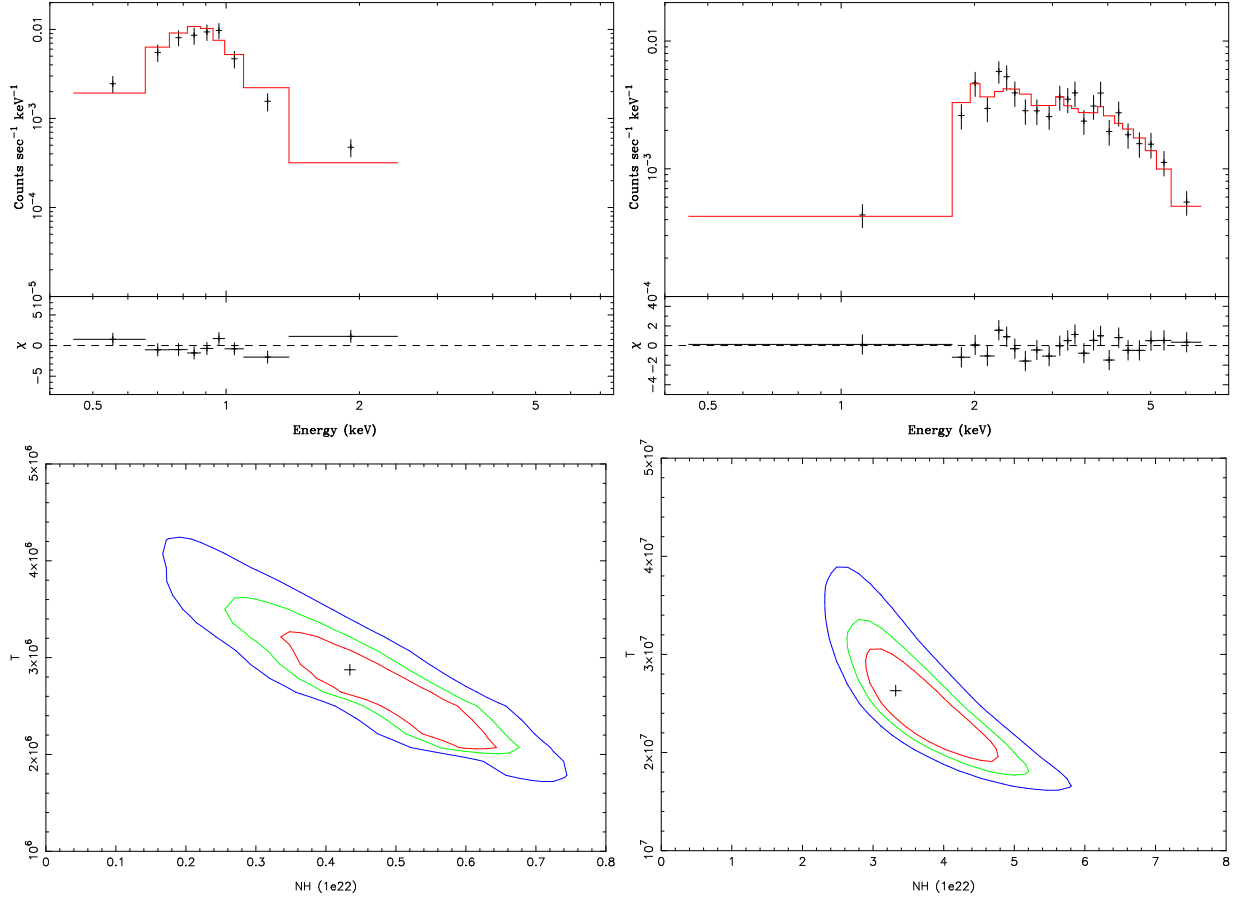


Fig. 7.— *Top*: Zero order spectrum of HD 104237-D (*left*) and E (*right*) with best fit model. The parameters of the best fit models are listed in Table 6. *Bottom*: Confidence contours in the N_H - T space (68%, 90%, 98%) for D (*left*) and E (*right*).

Table 1. Characteristics of HD 104237 members.

Object	Spec. Type ^a	EW(H α) ^b	offset ^c	comments
A ^d	A7.5Ve-A8Ve	-24.5	...	H α e, IR and UV excess, jets
B	M3-4	...	1.365'' \pm 0.019	IR excess
C	5.275'' \pm 0.033	BD (FLG03) or M6V (G04)
D	M2-3	-9	10''.72 \pm 0.05	H α near CTTS limit
E	K3IVe	-9	14''.88 \pm 0.05	H α near CTTS limit, IR excess

^aRanges of spectral types from Feigelson et al. (2003); Grady et al. (2004); Luhman (2004).

^bEquivalent width, in \AA , of H α emission from Acke et al. (2005); Grady et al. (2004).

^cfrom Grady et al. (2004).

^dA has a K3 spectroscopic companion within ~ 0.15 AU (Böhm et al. 2004) whose parameters are listed in Table 2.

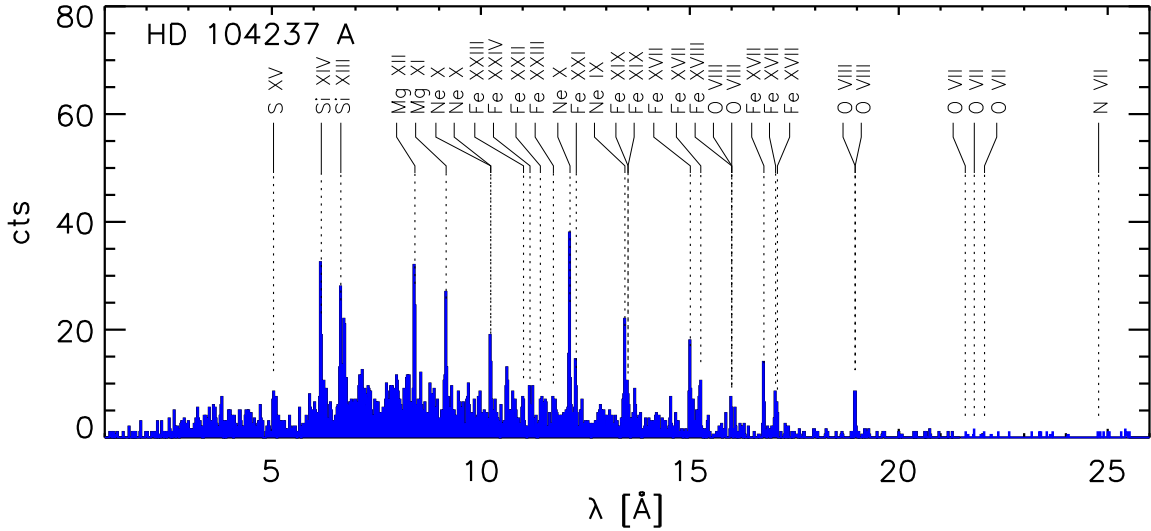


Fig. 8.— HD 104237-A *Chandra*-HETGS spectrum (HEG -1,+1, and MEG -1,+1 summed; binsize=0.02 \AA) integrated over the 145 ks observation. The most prominent lines are labeled.

Table 2. Characteristics of HD 104237-A and its spectroscopic companion.

Parameter	HD 104237-A	companion	Ref. ^a
d	116 pc		1
M_*/M_\odot	2.25	1.75	2
R_*/R_\odot	2.5 ± 0.2		3
$\log(L_*/L_\odot)$	$1.42^{+0.04}_{-0.07}$	0.5	2
$\log(T_{\text{eff}})$	3.87	3.675	2
Age	2-5 Myr		2,5
$v \sin i$	$12 \pm 2 \text{ km s}^{-1}$		4
i	$18^\circ_{-11}^{+14}, 23^\circ_{-8}^{+9}$		5,3
P_{rot} ^b	$100 \pm 5 \text{ hrs}$		3
P_{orb}	19.859 days		2
e ^c	0.66486		2

^aReferences: (1) Perryman et al. (1997); (2) Böhm et al. (2004); (3) Böhm et al. (2006); (4) Donati et al. (1997); (5) Grady et al. (2004).

^bPeriodicity of modulation observed in $H\alpha$, and possibly associated to rotational modulation by Böhm et al. (2006).

^cEccentricity of the binary orbit.

Table 3. Parameters of the HETG observations and count rates of X-ray sources HD 104237-A, B, C, D, E.

Obs ID	Start date and time	t_{exp} [ks]	count rate [cts/ks]					
			A		B ^a	C ^a	D ^a	E ^a
			0 th ^a	1 st ^b				
7319	2006-04-11 23:46:08	43.39	23.0	33.7	0.67	0.21	1.5	3.7
7320	2006-04-13 10:13:06	43.83	19.8	28.0	0.62	0.73	1.4	2.3
6444	2006-04-16 09:51:47	12.57	20.4	27.8	1.85	0.48	1.9	3.9
7326	2006-06-13 05:32:27	45.61	35.0	46.9	0.85	0.31	2.2	5.1

^acount rate from zero order counts in the 0.5-8 keV energy range.

^bcount rate from first order (MEG -1,+1, HEG -1,+1) dispersed counts, in the 1.5-26Å wavelength range.

These fluxes were determined by fitting each narrow ($\sim 0.5 \text{ \AA}$) region of interest with a sum of Gaussians and a plasma model continuum, all multiplied by a function of absorption by neutral gas with solar abundances. The model was folded through the instrument response for each of the negative and positive first orders for each grating, then the positive and negative orders were combined before computing the statistic. HEG and MEG orders were combined when feasible (roughly between 3-16 \AA , where the spectral coverage overlaps with significant sensitivity). The line widths were usually frozen at a negligible intrinsic value (in §4.3.3 we describe an independent analysis of line profiles). Only for O VIII 19 \AA did we need to free the width parameter; this is because of the high dispersion at this wavelength and the fact that the H-Ly α -like lines are doublets, with a separation of 0.006 \AA for O VIII.

The continuum model was determined by a prior fit of a three temperature-component continuum model to relatively line-free regions of the spectrum, using the Astrophysical Plasma Emission Database continuum emissivities (APED⁷; Smith et al. 2001). This continuum then became an *a priori* determined component for the line fits. For the absorption, we used the `wabs` function from the `XSPEC` module in `ISIS` and a fixed value of N_{H} (see §4.3). From these fits we obtained a single (unabsorbed) flux value as well as a wavelength.

We did not physically merge any data or response files into new files. Combination of the $\pm 1^{\text{st}}$ orders was done dynamically. There are many advantages to this technique. Foremost is that the individual responses are still applied to the model to compute the predicted counts for each order. Second, individual orders can be noticed and ignored as required for each region. Third, the combination after folding, and before the statistic, increases the signal-to-noise per bin (which does not occur for a joint fit). Fourth, the method is transparent to combination of orders from one observation or from multiple observations, since all responses, counts spectra, and exposure times are still unique. The visualization in Figure 8 shows the summed, combined, and rebinned HEG plus MEG counts spectrum, but this was not the object directly fit.

Since we have a fairly low-counts spectrum, we also regridded the data (and corresponding response) to the HEG binsize (0.0025 \AA). This allowed us to combine HEG and MEG spectra, but to keep HEG resolution in the HEG counts spectrum where feasible. Otherwise, we grouped data by an integral numbers of bins independently for each feature.

For Fe XXV (1.85 \AA), we also included the zeroth order spectrum in the fit, since the zeroth order has a comparable number of counts, and though lower resolution, there are no significant confusing lines.

⁷APED is available from <http://cxc.harvard.edu/atomdb/>

These dynamic functions for combining data, regridding responses and data, and for grouping data are standard features of ISIS.

Table 4. Parameters and uncertainties of 2-T models fitting the ACIS-I spectra of HD 104237-A.

Parameter ^a	ObsID 2404	ObsID 3428
T_1 (10^6 K)	4.7 [4.1-5.3]	4.8 [4.1-5.3]
EM_1 (10^{52} cm ⁻³)	19.6 [17.7-20.9]	22.9 [13.7-26.6]
T_2 (10^6 K)	36.8 [26.8-56.7]	18.8 [16.3-21.4]
EM_2 (10^{52} cm ⁻³)	3.4 [2.9-4.2]	15.4 [9.9-17.4]
L_s (10^{30} erg s ⁻¹)	2.7	4.1
L_t (10^{30} erg s ⁻¹)	3.0	4.7
HETGS modeled zero order count rate	0.020	0.035
ACIS-I modeled (unpiled) count rate	0.16	0.27
ACIS-I observed count rate	0.12	0.15

^aThe 1σ confidence intervals are listed in square brackets. N_H is fixed at 2×10^{21} cm⁻² and element abundances are fixed to the values derived from the HETGS spectrum (see Table 8). L_s and L_t are the X-ray luminosity values in the 0.5-2.0 keV and 0.5-8.0 keV respectively, as in FLG03; these value are corrected for absorption.

Table 5. Parameters and uncertainties of models fitting the zero-order spectrum of HD 104237-A.

Parameter ^a	I ^b	II ^c
	2T	2T
N_{H1} (10^{22} cm $^{-2}$)	0.17 [0.09-0.25]	0.12 [0.07-0.19]
T_1 (10^6 K)	4.7 [4.3-5.4]	5.0 [4.3-5.3]
EM_1 (10^{52} cm $^{-3}$)	16.4 [11.6-23.8]	11.4 [10.6-12.1]
N_{H2} (10^{22} cm $^{-2}$)	= N_{H1}	= N_{H1}
T_2 (10^6 K)	27 [24-31]	27 [24-30]
EM_2 (10^{52} cm $^{-3}$)	7.1 [6.0-8.5]	6.8 [6.3-7.4]
T_3 (10^6 K)	-	-
EM_3 (10^{53} cm $^{-3}$)	-	-
f_{X} (10^{-12} erg cm $^{-2}$ s $^{-1}$)	1.7 (1.1)	1.5 (1.1)
L_{X} (10^{30} erg s $^{-1}$)	2.9 (1.7)	2.4 (1.7)
O/ O_{\odot}	=0.65	0.46 [0.26-0.63]
Ne/ Ne_{\odot}	=1.1	1.7 [1.4-1.9]
Mg/ Mg_{\odot}	=0.66	1.1 [0.6-1.3]
Si/ Si_{\odot}	=0.91	1.2 [0.7-1.5]
S/ S_{\odot}	=1.24	1.4 [0.6-1.6]
Fe/ Fe_{\odot}	=0.50	0.42 [0.41-0.53]
χ_0^2 (d.o.f.)	1.12 (149)	1.05 (143)

^aThe 90% confidence intervals are listed in square brackets. For X-ray flux and luminosity (f_{X} , L_{X} ; derived in the 0.5-7.0 keV energy range) we list the value corrected for absorption, while the observed (absorbed) values are in parentheses. Abundances are relative to solar (Anders & Grevesse 1989).

^bModel with two temperature components and abundances fixed to the values found from the analysis of the high resolution spectra (see §4.3.1). This is our favored model.

^cModel with two temperature components and variable abundances.

Table 6. Parameters and relative uncertainties for isothermal models fitting the zero-order spectra of X-ray sources B, C, D, E.

Parameter	B	C	D	E
N_{H} (10^{22} cm $^{-2}$)	0.0 [0.0-0.8]	0.8 [0.-1.7]	0.44 [0.26-0.67]	3.4 [2.6-5.2]
T (10^6 K)	8.4 [1.8-10.]	7.0 [2.1-32.]	2.8 [2.0-3.6]	22. [18-34]
EM (10^{53} cm $^{-3}$)	0.085 [0.064-0.11]	0.13 [0.012-27.]	2.9 [0.5-18.]	1.8 [0.5-3.8]
f_{X} (10^{-13} erg cm $^{-2}$ s $^{-1}$)	0.35 (0.35)	0.4 (0.09)	6.5 (0.73)	7.1 (1.9)
L_{X} (10^{30} erg s $^{-1}$)	0.057 (0.057)	0.07 (0.0015)	1.0 (0.12)	1.1 (0.31)
χ_0^2	1.45	1.24	1.54	0.86
d.o.f.	13	2	6	20

Note. — The 90% confidence intervals are listed in square brackets. For X-ray flux and luminosity (f_{X} , L_{X} ; derived in the 0.5-7.0 keV energy range) we list the value corrected for absorption, while the observed (absorbed) values are in parentheses. For all sources the global metal abundances are fixed to 0.3 times solar.

Table 7. Line Measurements

Ion	Use ^a	$\overline{\log T^b}$	λ_t^c	λ_o^d	f_t^e	f_t^f	δf^g	$\delta \chi^h$
Fe xxv	E	7.8	1.861	1.868 (4.8)	1.15 (0.34)	0.712	0.441	1.30
Ar xviii	E	7.7	3.734	3.738 (15.)	0.18 (0.23)	0.154	0.025	0.11
Ar xvii	E	7.4	3.949	3.949 (8.5)	0.56 (0.47)	0.223	0.335	0.71
Ar xvii		7.3	3.968	3.953 (15.)	0.001 (0.37)	0.061	-0.060	-0.16
S xvi		7.5	3.992	4.007 (4.7)	0.26 (0.27)	0.249	0.006	0.02
S xv	E	7.3	4.088	4.088 (15.)	0.07 (0.18)	0.064	0.006	0.03
S xvi	E	7.6	4.730	4.729 (11.)	1.65 (0.85)	1.221	0.431	0.51
Si xiv	E	7.4	4.947	4.947 (-)	0.11 (0.19)	0.086	0.019	0.10
S xv	E	7.2	5.039	5.040 (2.0)	2.22 (0.61)	1.670	0.551	0.91
S xv	E	7.2	5.065	5.065 (-)	0.23 (0.32)	0.390	-0.160	-0.49
S xv	E	7.2	5.102	5.107 (5.8)	1.03 (0.46)	0.576	0.453	0.99
Si xiv	E	7.4	5.217	5.219 (2.8)	0.86 (0.46)	0.407	0.450	0.99
Si xiii		7.1	5.285	5.285 (-)	0.002 (0.18)	0.062	-0.059	-0.33
Si xiii	E	7.1	5.405	5.405 (-)	0.14 (0.29)	0.136	0.000	0.00
Si xiv	E	7.4	6.183	6.181 (2.1)	3.51 (0.88)	3.053	0.462	0.53
Si xiv		7.1	6.265	6.256 (15.)	0.45 (0.57)	0.072	0.374	0.65
Mg xii		7.2	6.580	6.580 (-)	0.001 (0.11)	0.063	-0.062	-0.59
Si xiii	E	7.0	6.648	6.650 (1.1)	3.63 (0.48)	3.609	0.018	0.04
Si xiii		7.0	6.687	6.687 (-)	0.18 (0.21)	0.688	-0.506	-2.44
Si xiii		6.8	6.720	6.720 (-)	0.60 (0.28)	0.035	0.561	2.02
Si xiii	E	7.0	6.740	6.743 (1.3)	2.06 (0.35)	1.465	0.594	1.69
Mg xii	E	7.2	7.106	7.107 (5.5)	0.83 (0.32)	0.458	0.370	1.15
Al xiii		7.4	7.171	7.167 (11.)	0.40 (0.28)	0.686	-0.284	-1.02
Mg xi		6.9	7.310	7.317 (6.8)	0.56 (0.31)	0.051	0.508	1.65
Fe xxii	E	7.1	7.681	7.667 (15.)	0.06 (0.19)	0.037	0.020	0.11
Al xii	E	7.0	7.757	7.761 (15.)	0.62 (0.37)	0.243	0.374	1.00
Al xii		6.9	7.805	7.790 (15.)	0.06 (0.19)	0.079	-0.015	-0.08
Mg xi	E	6.9	7.850	7.852 (5.8)	0.57 (0.33)	0.349	0.218	0.66
Al xii	E	6.9	7.872	7.879 (15.)	0.26 (0.30)	0.220	0.038	0.12
Fe xxiii		7.2	7.901	7.897 (15.)	0.33 (0.35)	0.062	0.267	0.76
Fe xxiv	E	7.4	7.986	7.988 (10.)	0.35 (0.38)	0.192	0.161	0.43
Fe xxiv	E	7.4	7.996	8.011 (7.5)	0.28 (0.29)	0.097	0.179	0.63
Fe xxiii	E	7.2	8.304	8.300 (11.)	0.28 (0.33)	0.229	0.052	0.16
Fe xxiv	E	7.4	8.316	8.317 (15.)	0.20 (0.31)	0.217	-0.018	-0.06
Fe xxiv		7.4	8.376	8.389 (-)	0.34 (0.34)	0.083	0.253	0.75
Mg xii	E	7.2	8.422	8.422 (1.6)	3.65 (0.50)	3.626	0.026	0.05
Fe XXI	E	7.1	8.574	8.567 (4.9)	0.58 (0.21)	0.188	0.395	1.88
Fe xxiii	E	7.2	8.815	8.816 (3.9)	0.69 (0.28)	0.247	0.447	1.59
Fe xxii	E	7.1	8.975	8.976 (6.6)	0.42 (0.28)	0.321	0.095	0.34
Mg xi	E	6.8	9.169	9.169 (1.3)	4.24 (0.78)	3.046	1.195	1.54
Fe XXI		7.1	9.194	9.194 (-)	1.14 (0.44)	0.144	0.994	2.24
Mg xi		6.8	9.230	9.230 (-)	1.39 (0.50)	0.489	0.895	1.80
Mg xi		6.8	9.314	9.315 (2.7)	2.20 (0.65)	1.447	0.755	1.17
Fe xxii		7.1	9.393	9.393 (-)	0.001 (0.20)	0.072	-0.071	-0.36
Ne x		7.0	9.481	9.472 (3.2)	0.48 (0.25)	0.379	0.096	0.38
Fe xix		6.9	9.695	9.680 (3.8)	0.72 (0.36)	0.122	0.601	1.66
Ne x	E	7.0	9.708	9.708 (-)	1.35 (0.61)	0.858	0.492	0.81
Fe xx	E	7.0	9.727	9.727 (-)	0.51 (0.39)	0.143	0.362	0.94
Ni xix	E	6.8	10.110	10.111 (9.6)	0.31 (0.36)	0.233	0.074	0.20

Table 7—Continued

Ion	Use ^a	$\overline{\log T^b}$	λ_t^c	λ_o^d	f_t^e	f_t^f	δf^g	$\delta\chi^h$
Fe XX	E	7.0	10.120	10.127 (14.)	0.39 (0.27)	0.161	0.232	0.87
Ne X	E	7.0	10.239	10.240 (1.7)	3.98 (0.83)	2.817	1.165	1.41
Fe XXIV	E	7.4	10.619	10.619 (-)	1.36 (0.60)	1.576	-0.217	-0.36
Fe XIX	E	6.9	10.641	10.641 (-)	1.05 (0.78)	0.273	0.772	1.00
Fe XIX	E	6.9	10.649	10.649 (-)	0.42 (0.60)	0.264	0.152	0.25
Fe XXIV	E	7.4	10.663	10.663 (-)	0.80 (0.58)	0.830	-0.026	-0.04
Fe XXIII		7.2	10.981	10.983 (13.)	0.39 (0.47)	1.443	-1.053	-2.26
Ne IX	E	6.7	11.001	11.001 (-)	1.23 (0.61)	0.418	0.812	1.33
Fe XXIII	E	7.2	11.019	11.019 (-)	1.34 (0.72)	0.953	0.382	0.53
Fe XXIV	E	7.4	11.029	11.029 (-)	1.25 (0.65)	1.047	0.205	0.32
Fe XVII		6.7	11.131	11.123 (15.)	0.001 (0.09)	0.810	-0.809	-8.82
Fe XXIV	E	7.4	11.176	11.176 (2.3)	2.72 (0.77)	1.915	0.799	1.04
Fe XVII	E	6.7	11.254	11.251 (2.8)	2.54 (0.76)	1.146	1.397	1.84
Fe XVIII	E	6.8	11.326	11.321 (4.5)	1.61 (0.64)	0.838	0.766	1.19
Fe XVIII	E	6.8	11.527	11.524 (6.8)	0.99 (0.61)	0.890	0.101	0.17
Ne IX	E	6.6	11.544	11.548 (4.9)	1.67 (0.69)	1.362	0.304	0.44
Fe XXIII		7.2	11.736	11.741 (1.8)	4.96 (0.99)	3.323	1.637	1.66
Fe XXII	E	7.1	11.770	11.773 (2.3)	3.34 (1.01)	3.561	-0.223	-0.22
Ne X	E	6.9	12.135	12.131 (1.0)	24.0 (2.9)	24.246	-0.254	-0.09
Fe XXIII		7.2	12.161	12.150 (4.2)	4.88 (2.05)	1.934	2.943	1.43
Fe XVII	E	6.7	12.266	12.265 (3.4)	3.60 (1.37)	3.113	0.483	0.35
Fe XXI	E	7.1	12.284	12.284 (2.1)	7.82 (1.75)	7.538	0.282	0.16
Fe XX	E	7.0	13.385	13.396 (6.5)	1.53 (1.17)	1.043	0.487	0.42
Fe XIX	E	6.9	13.423	13.423 (-)	2.57 (1.38)	0.559	2.008	1.46
Ne IX	E	6.6	13.447	13.449 (1.5)	15.2 (2.7)	12.577	2.657	1.00
Fe XIX	E	6.9	13.462	13.462 (-)	2.34 (1.73)	1.274	1.066	0.62
Fe XIX		6.9	13.497	13.497 (-)	0.36 (0.74)	2.245	-1.884	-2.54
Fe XIX	E	6.9	13.518	13.519 (1.9)	9.60 (2.34)	4.958	4.646	1.98
Ne IX		6.6	13.552	13.554 (3.3)	3.95 (1.57)	1.904	2.041	1.30
Fe XIX	E	6.9	13.645	13.653 (-)	1.49 (2.46)	0.801	0.687	0.28
Ne IX	E	6.6	13.699	13.694 (6.4)	6.91 (3.20)	6.299	0.607	0.19
Fe XX	E	7.0	13.767	13.762 (10.)	3.77 (3.37)	0.917	2.856	0.85
Fe XIX	E	6.9	13.795	13.790 (7.6)	3.90 (3.33)	2.036	1.863	0.56
Fe XVII	E	6.7	13.825	13.827 (11.)	3.92 (3.26)	2.787	1.129	0.35
Fe XVIII	E	6.8	14.208	14.207 (8.3)	9.60 (4.83)	12.652	-3.051	-0.63
Fe XVIII	E	6.8	14.256	14.249 (13.)	3.57 (3.68)	2.445	1.122	0.31
Fe XX	E	7.0	14.267	14.268 (13.)	3.59 (4.22)	1.561	2.030	0.48
Fe XVIII	E	6.8	14.343	14.355 (15.)	1.52 (3.24)	1.429	0.090	0.03
Fe XVIII	E	6.8	14.373	14.374 (5.4)	9.40 (3.77)	3.077	6.324	1.68
Fe XVIII		6.8	14.425	14.410 (15.)	3.49 (2.96)	0.668	2.821	0.95
Fe XVIII		6.8	14.534	14.547 (6.1)	4.36 (3.49)	2.365	1.999	0.57
Fe XIX	E	6.9	14.664	14.667 (11.)	4.95 (3.14)	1.558	3.389	1.08
O VIII	E	6.7	14.821	14.817 (4.4)	4.37 (1.78)	1.174	3.193	1.79
Fe XVII	E	6.7	15.014	15.014 (3.4)	32.8 (7.4)	39.169	-6.377	-0.86
Fe XIX	E	6.9	15.079	15.087 (9.2)	6.55 (6.59)	1.809	4.738	0.72
O VIII	E	6.7	15.176	15.178 (15.)	3.26 (6.12)	2.741	0.515	0.08
Fe XIX	E	6.9	15.198	15.209 (11.)	7.39 (6.26)	1.514	5.875	0.94
Fe XVII	E	6.7	15.261	15.261 (5.5)	17.3 (6.8)	11.351	5.939	0.87
Fe XVII	E	6.7	15.453	15.451 (15.)	4.26 (4.53)	1.484	2.778	0.61

4.3.1. Emission Measure Distribution and Abundances

We reconstructed an emission measure distribution (*EMD*) and elemental abundances by minimizing line flux residuals for features marked in Table 7 with an “E” in the “Use” column. This was an iterative process, since some features are blended or mis-identified: we excluded those with very large residuals during the fitting process. We also excluded the He-like resonance and intercombination lines since they are density dependent. Theoretical emissivities from APED were integrated over the temperature range of sensitivity after weighting by the trial *EMD* and abundances. The fit was subject to the constraint that the *EMD* be smooth. To obtain some estimate of the uncertainty in the reconstructed *EMD* and abundances, we performed 100 Monte-Carlo iterations in which the observed fluxes were randomly perturbed using a Gaussian distribution with their measurement uncertainties as the Gaussian σ . We computed the standard deviation in the resulting *EMD* at each temperature and for the abundances and use these for the fit uncertainty. This is not rigorously correct because it does not account for correlations in the allowed solutions. Other examples of this method, and further details, can be found in Huenemoerder et al. (2006, 2007), along with requisite caveats and limitations of emission measure modeling. As a final check, the synthetic spectrum was evaluated and compared to the observation (see Figure 10). Model line fluxes are listed in Table 7, the *EMD* is shown in Figures 9, and abundances are given in Table 8.

The emission measure distribution shown in Figure 9 is characterized by significant amount of plasma over a wide temperature range, as anticipated on the basis of a visual inspection of the spectrum, and by a peak at $\log T[K] \sim 6.9$. These characteristics are similar to the temperature distributions derived for several coronae of late-type stars (see e.g., Sanz-Forcada et al. 2003), typically presenting an emission measure peak around 10^7 K. However, coronae of active stars with X-ray luminosity $\gtrsim 10^{30} \text{erg s}^{-1}$ often present an additional significant peak at higher temperatures (a few 10^7 K) typically associated with flaring activity. Hot plasma is present in HD 104237-A as well, but with a lower relative weight than observed in other stellar coronae at a similar activity level.

In Figure 9 we also compare the *EMD* model with the $2T$ model obtained from the low-resolution spectra (model I in Table 5): the emission measure values for the components of the $2T$ model are scaled for comparison purposes, but their sum compares well with the integrated emission measure distribution. Figure 10 shows the synthetic spectrum from the *EMD* model, compared with the actual spectrum. Figure 11 compares the predicted spectrum from the two models with the actual observed spectrum and shows that while the overall characteristics of the $2T$ model are somewhat similar to the detailed *EMD* model, the latter reproduces the spectral features of the high-resolution spectrum much

Table 7—Continued

Ion	Use ^a	$\overline{\log T^b}$	λ_t^c	λ_o^d	f_t^e	f_t^f	δf^g	$\delta\chi^h$
Fe XVIII		6.8	15.494	15.488 (15.)	2.17 (3.32)	0.386	1.784	0.54
Fe XVIII	E	6.8	15.625	15.625 (15.)	2.51 (3.69)	3.604	-1.096	-0.30
Fe XVIII		6.8	15.759	15.763 (15.)	3.37 (4.31)	0.497	2.876	0.67
Fe XVIII	E	6.8	15.824	15.826 (15.)	4.60 (5.04)	2.251	2.346	0.47
Fe XVIII	E	6.8	15.870	15.875 (15.)	5.22 (5.49)	1.200	4.018	0.73
O VIII		6.7	16.006	16.004 (2.2)	21.7 (5.0)	9.436	12.242	2.43
Fe XVIII	E	6.8	16.071	16.075 (6.1)	4.22 (2.39)	5.304	-1.087	-0.45
Fe XIX		6.9	16.110	16.095 (2.5)	7.60 (2.97)	2.642	4.963	1.67
Fe XVIII		6.8	16.159	16.150 (4.0)	6.05 (2.49)	2.132	3.922	1.57
Fe XVII	E	6.7	16.780	16.779 (4.0)	41.4 (11.6)	21.558	19.810	1.71
Fe XVII	E	6.7	17.051	17.052 (6.3)	29.4 (10.9)	26.525	2.838	0.26
Fe XVII	E	6.7	17.096	17.100 (4.4)	37.8 (11.2)	24.814	13.014	1.16
Fe XVIII		6.8	17.623	17.635 (4.7)	6.14 (3.39)	4.127	2.010	0.59
O VII		6.4	17.768	17.762 (8.1)	4.87 (3.26)	0.663	4.203	1.29
Fe XVII	E	6.6	17.793	17.778 (15.)	0.001 (1.48)	0.000	0.000	0.00
O VII		6.4	18.627	18.627 (-)	0.001 (1.24)	2.329	-2.328	-1.87
Ca XVIII	E	7.1	18.691	18.691 (-)	0.46 (3.05)	0.644	-0.185	-0.06
O VIII	E	6.7	18.970	18.971 (2.2)	104. (17.)	89.094	14.826	0.85
Ca XVI		6.7	20.859	20.869 (12.)	7.09 (7.70)	0.043	7.046	0.92
N VII		6.5	20.910	20.881 (30.)	0.001 (5.28)	1.958	-1.958	-0.37
O VII	E	6.3	21.601	21.605 (10.)	20.0 (16.3)	28.511	-8.519	-0.52
O VII		6.3	21.802	21.817 (6.4)	17.3 (15.3)	3.861	13.392	0.88
O VII		6.3	22.098	22.083 (15.)	2.20 (9.83)	16.800	-14.603	-1.49
N VII	E	6.5	24.782	24.797 (15.)	20.4 (14.3)	13.131	7.253	0.51

^aThe label E indicates the lines used for the emission measure reconstruction.

^bAverage logarithmic temperature (kelvins) of formation.

^cTheoretical wavelengths of identification (from APED), in Å units. If the line is a multiplet, we list the wavelength of the strongest component.

^dMeasured wavelength, in angstrom units (uncertainty is in mÅ). Errors equal to (-) indicate that the line wavelength was frozen because the feature is very weak.

^eMeasured line fluxes in 10^{-6} photons $\text{cm}^{-2} \text{s}^{-1}$ for HEG+MEG first orders, with 1σ uncertainties, assuming $N_{\text{H}} = 1.5 \times 10^{21} \text{ cm}^{-2}$.

^fFluxes (in 10^{-6} photons $\text{cm}^{-2} \text{s}^{-1}$) predicted using the emission measure distribution model (see Fig. 9).

^gLine flux residuals, $\delta f = f_l - f_t$.

^hDiscrepancy between observed and predicted fluxes in units of σ .

more satisfactorily.

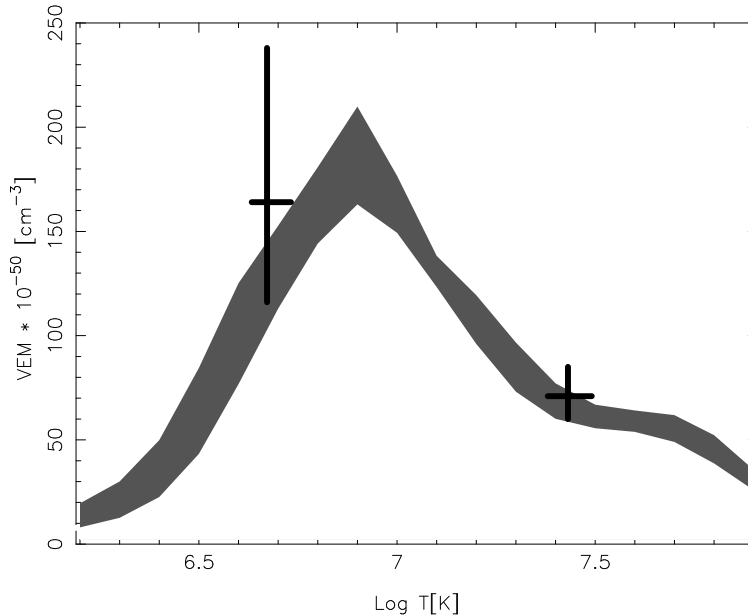


Fig. 9.— Emission measure distribution inferred from the measured line fluxes. Crosses show the EM component derived from the $2T$ fit to zero-order spectra. Since we are plotting the emission measure integrated over the temperature bins, we applied an arbitrary scaling factor of 0.1 to the $2T$ models in order to compare the relative weights with the shape of the EMD; total volume emission measures for the two models, $2T$ and EMD , are comparable, as they should be.

The element abundances of the X-ray emitting plasma of HD 104237-A derived from the analysis of its HETGS spectrum are listed in Table 8, both compared to solar values (Grevesse & Sauval 1998) and to the photospheric values of HD 104237-A from Acke & Waelkens (2004). These abundances show a general depletion of elements in the X-ray emitting plasma with the exception of S, generally in line with X-ray studies of other PMS stars (e.g., Maggio et al. 2007), however with some possible differences: the Ne/Fe abundance ratio is relatively low (~ 2), with respect to the extremely high values observed in other young stars (see e.g., Kastner et al. 2002; Argiroffi et al. 2005 finding values of Ne/Fe ~ 10 for PMS stars in TWA); also, possible dependence of fractionation on the element first ionization potential, as often observed in coronae of late-type stars (e.g., Telleschi et al. 2005), is not obviously present in the X-ray emitting plasma of HD 104237-A.

Table 8. Element abundances of X-ray emitting plasma from high resolution spectrum.

Element	A/A_{\odot}^a	A/A_{phot}^b	$A_{\text{phot}}/A_{\odot}$ [dex] ^c
O	0.65 ± 0.14	0.82 ± 0.33	-0.10 ± 0.14
Ne	1.05 ± 0.10
Mg	0.66 ± 0.08	1.02 ± 0.20	-0.19 ± 0.07
Si	0.91 ± 0.10	$0.87 \pm 0.25/0.45 \pm 0.11$	$0.02 \pm 0.11/0.31 \pm 0.09$
S	1.24 ± 0.36	1.75 ± 0.80	-0.15 ± 0.14
Fe	0.50 ± 0.05	0.42 ± 0.19	0.08 ± 0.18

^aElement abundances of the X-ray emitting plasma from the high resolution X-ray spectrum, expressed as relative to solar (Grevesse & Sauval 1998). We also list 1σ errors.

^bElement abundances of the X-ray emitting plasma from the high resolution X-ray spectrum, expressed as relative to photospheric abundances. Errors are calculated propagating the errors on both the photospheric abundances, and the abundances of the X-ray emitting plasma.

^cPhotospheric values of element abundances from Acke & Waelkens (2004); for Si we list their values derived from Si I, and from Si II respectively.

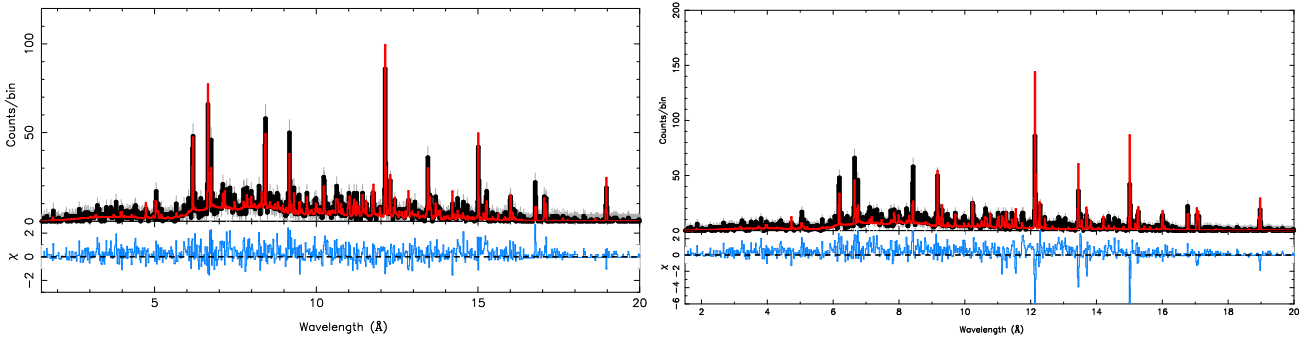


Fig. 11.— Comparison of the HEG+MEG spectrum of HD 104237-A with the spectrum simulated using the *EMD* model (*left*) and the *2T* model (*right*). Note the different scales on χ .

4.3.2. Density and Temperature Diagnostics from Line Ratios

The He-like triplets, in particular the cooler Ne IX and O VII triplets, thanks to their sensitivity to plasma density and temperature (e.g., Gabriel & Jordan 1969), and to photoexcitation from possible UV field, provide effective diagnostics for the X-ray emission mechanism in young stars (e.g., Kastner et al. 2002). In particular, in absence of intense UV field, the ratio of the forbidden to intercombination line, $R \equiv f/i$, is sensitive to plasma densities above a critical density value that depends on the element and increases from approximately $3 \times 10^{10} \text{ cm}^{-3}$ for O VII to about $3 \times 10^{13} \text{ cm}^{-3}$ for Si XIII. The presence of strong UV field, either photospheric for hot stars or produced in accretion shocks in young stars, affects the R ratio similarly to high densities, i.e. decreasing its value. In the case of HD 104237-A the stellar effective temperature is low enough (see Table 2) to rule out any effect of the photospheric UV field on the X-ray triplet lines. The ratio of the summed forbidden and intercombination lines with the resonance line, $G \equiv (f+i)/r$, provides instead a temperature diagnostic (though with some caveats on the reliability of the diagnostics, as discussed e.g., by Testa et al. 2004).

The O VII He-like triplet at 22\AA is too weak in HETGS spectrum of HD 104237-A to provide any meaningful diagnostic (only 3 counts are detected for the strongest triplet line, the 21.6\AA resonance line). Ne IX, Mg XI, and Si XIII have good signal-to-noise ratios and provide useful info on the plasma density and temperature. The Si XIII triplet is at the low density limit as for all other observed high resolution spectra of late-type stars (e.g., Testa et al. 2004).

In Figure 12 we show the Ne IX and Mg XI triplet regions with our best fit parametric models (upper panels), and the confidence contours in the parameter space of the line ratios R and G (lower panels). In the R and G parameter space we overplot the grid of corresponding densities and temperature according to Smith et al. (2001). The fitting model for the Ne IX triplet region includes the blends of mostly Fe lines as computed from the *EMD* model (see e.g., Huenemoerder et al. 2006). The best fit to the Ne IX triplet lines corresponds to a density $n_e \sim 6 \times 10^{11} \text{ cm}^{-3}$; however the relatively low statistics of the spectrum does not allow to put stringent limits on this value and we can reliably derive only an upper limit to the density of about $n_e \lesssim 6 \times 10^{12} \text{ cm}^{-3}$.

The fits to the Mg XI triplet region included Ne X Ly series blends, and blends of Fe lines (see e.g., Testa et al. 2004). Mg XI allows to put slightly better constraints on the plasma density: the best fit density is $n_e \sim 7 \times 10^{12} \text{ cm}^{-3}$ with a 1σ interval $1 - 18 \times 10^{12} \text{ cm}^{-3}$, somewhat high compared with typical values of active late-type stars (e.g., Testa et al. 2004). Also the G ratio is somewhat extreme when compared with typical coronal values, being at the low-end of the range of measured ratios (Testa et al. 2004), even though the rather

large uncertainties do not allow to draw definite conclusions. Interpreting the G ratio as a temperature diagnostics would point to a plasma temperature in agreement with the expected values for the formation of these lines. This is at variance with findings relative to He-like triplets of stellar coronae whose G ratios generally underestimate the plasma temperature. Therefore it is difficult to interpret an unusually low G ratio in HD 104237-A as a temperature effect considering that its temperature structure does not seem peculiar when compared to stellar coronae. We note that also the Ne IX G ratio has a value among the lowest measured in a large sample of active stars at different activity levels (Ness et al. 2004).

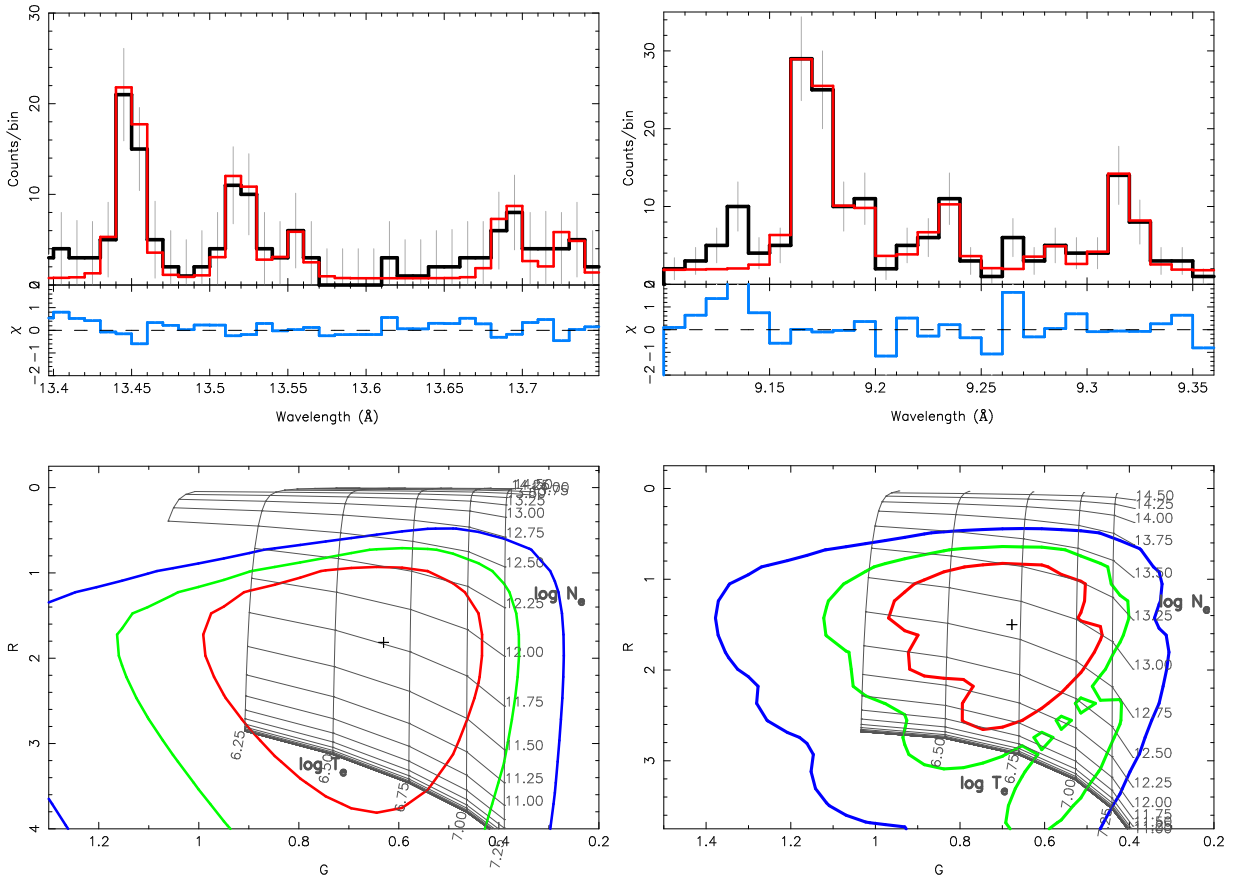


Fig. 12.— *Chandra*-HETGS spectrum of HD 104237-A in the Ne IX (*left*) and in the Mg XI (*right*) He-like triplet wavelength regions (black; rebinned by a factor 2 with respect to original wavelength grid) with best fit model (red). The lower panels show the corresponding confidence contours (68%, 90%, 98%) in the $R-G$ parameter space and indicate the density and temperature diagnostics derived from the triplet line ratios.

4.3.3. Line profiles

Spectral line profiles in X-rays allow us to probe the bulk velocity of hot plasma and its turbulent state. We carried out the measurement of line centroid positions of several prominent emission lines detected in the MEG spectra with sufficient counts for meaningful fits.

The methodology used here is somewhat different from the line-flux measurements described in §4.3. Line centroids are very sensitive to blending, even with weak features. Here we take advantage of a model spectrum which predicts the relative positions and relative strengths of many features in any region. Including thermal broadening in the flux evaluation automatically accounts for any line-width difference between species, and turbulent broadening can be included to test for excess width. For the best accuracy, these fits were only done on strong-line regions, whereas flux measures for emission measure reconstruction were also done for weak lines, since the absence of a line can be significant for the temperature structure. Since the line widths are barely resolved, if at all, the width measurement can best be done on only the highest signal-to-noise features, and though the HEG has higher spectral resolution, the higher counts in the MEG can make its determination of width more significant.

Utilizing the latest calibration product for MEG line spread function (available for *Chandra* CALDB v.3.4.0 or higher), grating ARFs and RMFs are generated for MEG +1 and -1 orders. Then the ± 1 order MEG spectra are simultaneously fit with a simple 2T model similar to the ones listed in Table 5 (close to model I) with line centroid and broadening parameters as free parameters. We have taken thermal broadening into account upon fitting. Since the observations were taken at four different times over the two-month period, each spectrum was corrected for appropriate barycentric motion of the Earth (-8.3 , -9.9 , -9.4 , and $+13$ km s $^{-1}$ for ObsID 6444, 7319, 7320 and 7326, respectively) prior to the fitting process.

We selected eight prominent lines in a wavelength range from 6 to 20Å: the H-like Ly α transitions of Si, Mg, Ne, and O, and the Fe XVII transitions at ~ 15.0 and 17.1Å. The measured line velocities are tabulated in Table 9.

The mean line centroid velocity of the source is 46 ± 42 km s $^{-1}$ with a 99% confidence level. The large uncertainty in the measurement results from the low S/N level detected in each emission lines. As noted, HD 104237-A is a binary system. Generally a small radial velocity correction should be made – prior to line fitting – for a spectrum obtained at each epoch. However, we intentionally neglect this since (i) we do not know the relative contribution of each component to the spectra and (ii) all of the spectra were obtained in the phase ranging from 0.25 – 0.5 (see bottom panel of Figure 4), placing the stars near

apastron where the change in radial velocity happens to be very small, of order of 7 km s^{-1} based on Böhm et al. 2004.

At the observed times, the radial velocity of the primary star, the HAe star, should be observed at $\approx +20 \text{ km s}^{-1}$, whereas the companion, K3, should be at $\approx +10 \text{ km s}^{-1}$. While the measured radial velocity prefers the primary star to be the source of hard X-rays, the companion is not statistically ruled out as the source. Furthermore, with the radial velocity correction of the systemic binary motion, the measured line centroid velocity becomes consistent with the hard X-ray source being at rest.

We also measured the width of the lines, using MEG ± 1 (and HEG ± 1 for lines with sufficient counts like the Ne X Ly α transition) order spectra. The line widths are consistent with zero broadening for all the strongest lines, with upper limit for v_{turb} of the order of 300 km s^{-1} . The fit to the Fe XVII 15\AA line provides a best fit width corresponding to a turbulent velocity v_{turb} of about 280 km s^{-1} , and barely compatible with 0 at the 99% level. However, we note that the statistics are limited, and a small error in the continuum can cause v_{turb} to be compatible with 0 at the 68% confidence level. Also, the other Fe XVII lines around 17\AA are compatible with zero broadening casting doubts on the results to the fit to the 15\AA line.

5. Discussion

The HD 104237 young association, with presumably coeval stars spanning $0.15\text{--}2.3M_{\odot}$, offers a laboratory for studying X-ray emission in young low/intermediate mass stars. The brightest X-ray source (and also so in optical, UV, and IR bands) in the stellar group is a system harboring a binary of intermediate mass stars ($2.25/1.75 M_{\odot}$) with a HAe star, and a slightly lower mass star in an early evolutionary stage with spectral type K3. The Herbig Ae star HD 104237-A with its proximity, high L_X , and low line-of-sight extinction is one of the few HAe stars accessible to high resolution X-ray spectroscopy, allowing us to investigate the nature of the X-ray emission from young intermediate mass stars that is still a mystery. The age of the binary system is estimated between 2 and 5 Myr (Böhm et al. 2004, FLG03), and the HAe star is correspondingly in the late stages of its pre-main sequence phase.

The long *Chandra*-HETGS observation provides important clues to the X-ray emission mechanism through spectral diagnostics and variability. Different scenarios may be considered to explain the X-ray emission of HD 104237-A: (1) all X-ray emission comes from the HAe star; (2) all X-ray emission comes from the companion; (3) both binary components contribute to the observed X-ray emission. The companion hypothesis is still considered a

viable explanation for the X-ray emission of Herbig Ae stars, considering that these intermediate mass stars are not expected to produce X-rays either through wind shocks, as in earlier type stars, because their winds are weak, or through magnetic activity as in later type stars, because they should not have an efficient solar-like dynamo mechanism producing magnetic fields since they lack sizable convective zones. However, some alternative mechanisms might be at work in the early stages of their evolution: (i) X-ray emission from accretion shocks, as in some classical T Tauri stars (e.g., Kastner et al. 2002), (ii) coronal activity due to non-solar dynamo mechanism (Tout & Pringle 1995), (iii) magnetically confined winds (Babel & Montmerle 1997). All these mechanisms require the presence of some sizable magnetic field in this evolutionary stage. The magnetic field in HAe stars has been investigated on large sample of these intermediate mass stars, and a small number of them do show evidence of magnetic fields of strength from a few tens of Gauss to a few hundreds of Gauss in a few cases (Donati et al. 1997; Hubrig et al. 2004; Wade et al. 2005, 2007; Hubrig et al. 2007; Catala et al. 2007). HD 104237-A is one of those showing that, whatever the mechanism that generates it, at some stage these intermediate mass stars can have magnetic fields. The expected X-ray properties are different depending on the mechanisms with (i) characterized by soft X-rays emitted by high density plasma, and harder X-ray emission due to magnetic confinement (and presumably heating) in (ii), and (iii). In particular in the scenario of coronal activity we expect a large degree of variability and flare-like dynamic events.

What do we know from observations of other HAe stars? X-ray observations with *Chandra* allow to resolve the Herbig Ae stars from close ($\gtrsim 1''$) companions and therefore reduce the confusion, and still indicates that a significant fraction ($\sim 35\%$; Stelzer et al. 2006) of Herbig Ae star with unknown companions are X-ray sources. As shown by Stelzer et al. (2006), the HAe stars have X-ray properties (L_X , T) very similar to lower mass young stars; therefore they conclude that either their emission and, likely, X-ray production mechanisms are very similar to TTS (i.e., coronal), or their X-ray emission comes from yet to be discovered companions. A few exceptions exist: HD 163296 has been observed with *Chandra* and shows an unusually soft spectrum, that Swartz et al. (2005) tentatively attribute to accretion shocks as in some CTTS; analogously AB Aur shows a very soft spectrum (Telleschi et al. 2007).

The spectroscopic companion to HD 104237-A is a later spectral type star (similar to SU Aur) and similar stars are known to be strong X-ray emitters (see e.g., Getman et al. 2005, and Güdel et al. 2007). Therefore the K3 companion is expected to contribute significantly to the overall X-ray emission. We explore the companion hypothesis assuming that the X-ray emission is entirely due to the K-type companion to HD 104237-A, and comparing its properties with the X-ray properties of stars of similar mass and evolutionary stage. The *Chandra* Orion Ultradeep Project (COUP; Getman et al. 2005) provides information for putting the X-ray emission properties of the HD 104237 members into context. In Figure 13

we compare some spectral properties of the HD 104237 members with the large sample from COUP (Preibisch et al. 2005). In particular Preibisch et al. (2005) analyzed the *Chandra*-ACIS spectra of the COUP sources with a two-temperature model and studied how the best fit temperatures change with spectral type. We superimpose on the results from COUP our temperature values from the modeling of the zero-order spectra, assuming a spectral type K3 for HD 104237-A (Figure 13, left panel). We analyze in the same context also the results found for source D and E, which have well determined spectral types.

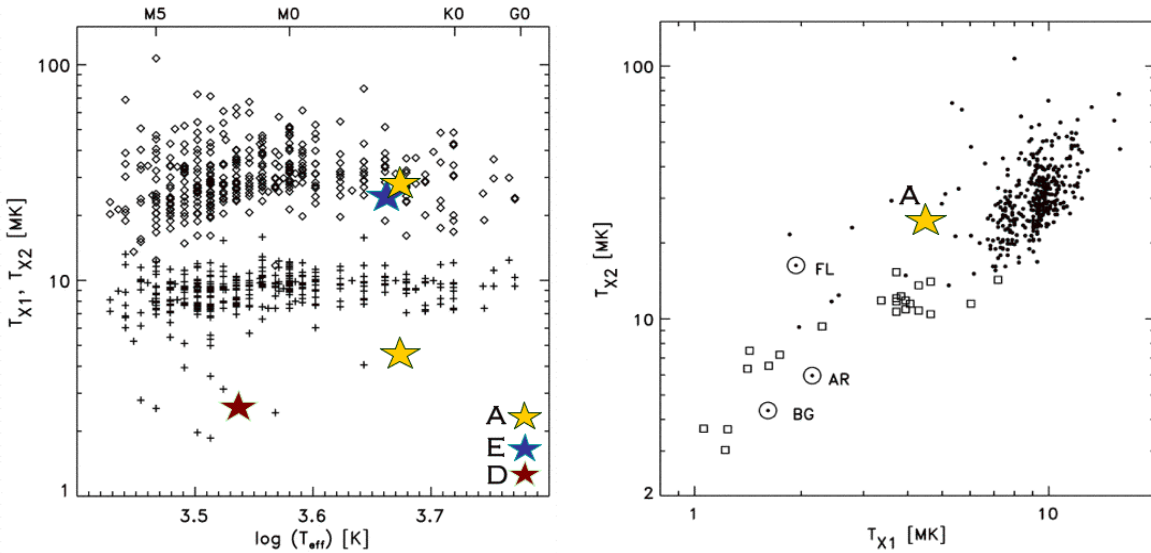


Fig. 13.— Comparison of plasma temperature of the HD 104237 members, obtained from 2-T (for source A) or 1-T (for source D, and E) analysis of their zero-order spectra, with results from the COUP sample (Preibisch et al. 2005). We used plots from Preibisch et al. (2005) (their Fig. 12, and 13; reproduced by permission of the AAS) and superimposed the values found for HD 104237-A, D and E (star symbols of different colors: A = yellow, D = red, and E = blue). *Left panel:* temperature of X-ray emitting plasma vs. effective temperature. T_{X1} (crosses), and T_{X2} (diamonds) are the two temperature values of a 2-T model fit to the low resolution X-ray spectra. *Right panel:* T_{X1} vs. T_{X2} . Preibisch et al. (2005) (see references therein) include in the plot results for a sample of G- and K-type MS stars (open squares), and typical values for structures in the solar corona (BG = background corona; AR = active region; FL = flares).

The plots of Figure 13 show that the hotter of the two temperatures fitting the spectrum of source A compares well with the high temperature component found for early K-type stars in the young star forming region of Orion, and also with the temperature of source E which has same spectral type as the spectroscopic binary companion to A. On the other hand, the soft component seems significantly cooler than the soft component of these similar stars.

This soft component is reminiscent of the soft spectra found for the two Herbig Ae stars, HD 163296 and AB Aur (Swartz et al. 2005; Telleschi et al. 2007). These recent findings might lend support to the idea that characteristic soft X-ray emission could be a defining property of X-ray spectra of HAe stars. The persistent hot component, however, cannot be explained by either the wind models or magnetic infall scenario proposed for the CTTS, and therefore the detection of the hot component suggests the presence of magnetically confined plasma. This hot emission is likely produced, at least partially, by the later type companion; on the other hand the X-ray emission mechanisms – emission from magnetically confined coronal plasmas, or from accretion streams, or from magnetically confined winds – may not be mutually exclusive and may all contribute to the X-ray emission in some HAe systems. Possible generation of magnetic fields in HD 104237-A cannot be easily explained with existing models. The estimated position in the HR diagram and evolutionary tracks imply that HD 104237-A is already completely radiative and therefore it should not be able to produce any magnetic field by solar-like dynamo mechanism. In the alternative shear magnetic model by Tout & Pringle (1995), X-ray luminosities at levels high enough to explain the observed L_X of HAe stars can be produced for time scales of the order of 1 Myr, and then they are rapidly decreasing as $L_X(t) = L_{X_0}(1 + t/t_0)^{-3}$, where L_{X_0} depends on the stellar parameters. As calculated by Skinner et al. (2004) depending on the set of stellar parameters adopted in the ranges discussed in §2 this model underestimates the observed L_X by a factor ~ 4 (for spectral type A4Ive and age $t \sim 2$ Myr) to ~ 25 (for the more recently determined spectral type A7.5ve-A8ve and age 2-5 Myr).

HD 163296, AB Aur and HD 104237-A show similar level of X-ray emission with fractional luminosity $\log L_X/L_{\text{bol}}$ of about -5.5 (Swartz et al. 2005), -5.6 (Telleschi et al. 2007), and -5 (this work; $\log L_X/L_{\text{bol}} \sim -4$ if we assume that the K3 companion is the X-ray source) respectively. Another similarity between HD 104237-A and AB Aur consists in their X-ray variability: both sources are slowly varying within a factor ~ 2 , do not present any clear evidence of flaring activity, and their X-ray lightcurve is compatible with their respective rotational period as derived from periodicity of optical lines. The HETGS observations presented in this paper do not provide enough phase coverage to definitely determine the presence of X-ray modulation on the timescales of modulation of the $H\alpha$ line, however, if the observed modulation is confirmed to be consistent with the rotation period of the HAe star, this would imply that a significant portion of the observed X-ray emission is produced by the HAe star. X-ray rotational modulation has been previously observed in a number of X-ray bright PMS stars, such as for instance by Flaccomio et al. (2005) who found evidence of X-ray emission being modulated by rotation in at least 10% of the Orion PMS stars sample observed in the COUP campaign; these findings are also compatible with theoretical modeling of TTS coronae from extrapolations of surface magnetograms derived from

Zeeman-Doppler imaging (Gregory et al. 2006).

The high resolution HETGS spectra offer additional spectral diagnostics providing clues to the yet unestablished X-ray production mechanisms in young intermediate mass stars. Particularly useful diagnostics are provided by the He-like triplets: specifically the Ne IX and Mg XI triplets, since the O VII triplet is essentially undetected, and the Si XIII lines are at the low density limit (therefore providing only an upper limit to density of a few 10^{13} cm^{-3}). Both Ne and Mg He-like triplets line ratios indicate plasma densities somewhat larger than typically observed in stellar coronae at the same level of activity, though the limited statistics do not provide very stringent constraints to these findings. In the scenario tentatively drawn above, with the Herbig Ae star being the main contributor to the cool ($< 10^7 \text{ K}$) emission and the K3 companion producing most of the hard emission, these triplets lines would be produced mainly by the Herbig Ae star. Considering the presence of significant ongoing accretion (at an estimated rate of $\sim 10^{-8} M_{\odot} \text{ yr}^{-1}$), in analogy with TW Hya and other accreting T Tauri stars showing high density in their high resolution spectra (e.g., Kastner et al. 2002; Stelzer & Schmitt 2004; Schmitt et al. 2005; Günther et al. 2006; Argiroffi et al. 2007), the high densities observed for HD 104237-A can be interpreted as a signature of X-ray production in accretion shocks. The high resolution spectra also provide line profile diagnostics potentially able to determine the contribution to the X-ray emission of each component of a binary system (see e.g., Ishibashi et al. 2006). We find that the measured line centroids for the strongest lines (see §4.3.3) indicate that the Herbig Ae star is more likely, with respect to the K3 companion, to be the primary X-ray source. However, in our case the involved velocities are small, and the statistics limited, therefore not providing conclusive results. As discussed in §4.3.3 no convincing evidence of line broadening is found in the strong X-ray lines.

Among the other sources in the association, source D shows interesting characteristics: as clear from Figure 13 (left panel), source D is characterized by an unusually cool plasma temperature with respect to the bulk of similar M-type young stars in Orion. Even though no clear evidence of ongoing accretion is available for this star, its H α emission is near the CTTS limit indicating that this star might still be actively accreting from its circumstellar disk; in this scenario, the soft excess might indicate that X-rays produced by shocked accreting plasma dominate the X-ray emission of this star, analogously to the peculiar case of TW Hydrae (Kastner et al. 2002), and differently from the majority of TTS where the coronal component generally dominates the overall X-ray emission (e.g., Preibisch et al. 2005).

6. Conclusions

We have analyzed *Chandra*-HETG observations of young low-mass and intermediate-mass stars in the small stellar group associated with the Herbig Ae star HD 104237 to investigate the X-ray emission mechanisms in their pre-main sequence phase. The close (~ 15 AU) binary system of the HAe star and its K-type companion cannot be resolved in X-rays, however our findings with respect to the X-ray variability and spectral properties provide clues to the origin of the X-ray emission and the X-ray production mechanisms. The modulation on time scales of the estimated rotation period of the HAe star suggests that the primary contributes significantly to the observed X-ray emission. The spectral analysis reveals a strong soft component (~ 0.5 keV) significantly cooler than typically found in K-type stars of evolutionary stage similar to that of the HD 104237-A companion (0.7 – 1 keV). We interpret these findings in a possible scenario where the soft X-rays are produced mainly by the HAe star and the hard emission by the later-type companion. The analysis of the HETGS spectrum provides additional diagnostics, in particular through the He-like triplets: the line ratios of the Mg XI and Ne IX triplets suggest the presence of plasma at high densities of about 10^{12} cm $^{-3}$, possibly indicating accretion related X-ray production mechanism.

The observed X-ray emission of the other sources is typical of pre-main sequence stars of similar ages and spectral types, except for the M-type T Tauri star HD 104237-D for which we find evidence of remarkably soft emission, with temperature of 3 MK reminiscent of the X-ray emission of the classical T Tauri star TW Hya whose emission is attributed to shocks in the accreting plasma.

This research was supported by SAO contract SV3-73016 to MIT for support of the *Chandra X-ray Center*, which is operated by SAO for and on behalf of NASA under contract NAS8-03060. This research was based on Chandra Cycle 7 Guaranteed Time Observation program selected by Claude Canizares, whom we thank for providing the opportunity to analyze these data, and for useful discussions and comments on this manuscript.

REFERENCES

- Acke, B., van den Ancker, M. E., & Dullemond, C. P. 2005, *A&A*, 436, 209
- Acke, B., & Waelkens, C. 2004, *A&A*, 427, 1009
- Alcala, J. M., Krautter, J., Schmitt, J. H. M. M., Covino, E., Wichmann, R., & Mundt, R. 1995, *A&AS*, 114, 109

- Anders, E., & Grevesse, N. 1989, *Geochim. Cosmochim. Acta*, 53, 197
- Appenzeller, I. 1994, in *Astronomical Society of the Pacific Conference Series*, Vol. 62, *The Nature and Evolutionary Status of Herbig Ae/Be Stars*, ed. P. S. The, M. R. Perez, & E. P. J. van den Heuvel, 12–+
- Argiroffi, C., Maggio, A., & Peres, G. 2007, *A&A*, 465, L5
- Argiroffi, C., Maggio, A., Peres, G., Stelzer, B. & Neuhäuser, R. 2007, *A&A*, 439, 1149
- Babel, J., & Montmerle, T. 1997, *A&A*, 323, 121
- Bernasconi, P. A., & Maeder, A. 1996, *A&A*, 307, 829
- Blondel, P. F. C., & Djie, H. R. E. T. A. 2006, *A&A*, 456, 1045
- Böhm, T., Catala, C., Balona, L., & Carter, B. 2004, *A&A*, 427, 907
- Böhm, T., Dupret, M. A., & Aynedjian, H. 2006, *Memorie della Societa Astronomica Italiana*, 77, 362
- Canizares, C. R., Davis, J. E., Dewey, D., Flanagan, K. A., Galton, E. B., Huenemoerder, D. P., Ishibashi, K., Markert, T. H., Marshall, H. L., McGuirk, M., Schattenburg, M. L., Schulz, N. S., Smith, H. I., & Wise, M. 2005, *PASP*, 117, 1144
- Catala, C., Alecian, E., Donati, J.-F., Wade, G. A., Landstreet, J. D., Böhm, T., Bouret, J.-C., Bagnulo, S., Folsom, C., & Silvester, J. 2007, *A&A*, 462, 293
- Damiani, F., Micela, G., Sciortino, S., & Harnden, Jr., F. R. 1994, *ApJ*, 436, 807
- D’Antona, F., & Mazzitelli, I. 1994, *ApJS*, 90, 467
- Davis, J. E. 2001, *ApJ*, 562, 575
- Donati, J.-F., Semel, M., Carter, B. D., Rees, D. E., & Collier Cameron, A. 1997, *MNRAS*, 291, 658
- Drake, J. J., Testa, P., & Hartmann, L. 2005, *ApJ*, 627, L149
- Feigelson, E. D., Lawson, W. A., & Garmire, G. P. 2003, *ApJ*, 599, 1207
- Flaccomio, E., Micela, G., Sciortino, S., Feigelson, E. D., Herbst, W., Favata, F., Harnden, Jr., F. R., & Vrtilik, S. D. 2005, *ApJS*, 160, 450

- Fruscione, A., McDowell, J. C., Allen, G. E., Brickhouse, N. S., Burke, D. J., Davis, J. E., Durham, N., Elvis, M., Galle, E. C., Harris, D. E., Huenemoerder, D. P., Houck, J. C., Ishibashi, B., Karovska, M., Nicastro, F., Noble, M. S., Nowak, M. A., Primini, F. A., Siemiginowska, A., Smith, R. K., & Wise, M. 2006, in Presented at the Society of Photo-Optical Instrumentation Engineers (SPIE) Conference, Vol. 6270, Observatory Operations: Strategies, Processes, and Systems. Edited by Silva, David R.; Doxsey, Rodger E.. Proceedings of the SPIE, Volume 6270, pp. 62701V (2006).
- Gabriel, A. H., & Jordan, C. 1969, MNRAS, 145, 241
- Garcia Lopez, R., Natta, A., Testi, L., & Habart, E. 2006, A&A, 459, 837
- Getman, K. V., Flaccomio, E., Broos, P. S., Grosso, N., Tsujimoto, M., Townsley, L., Garmire, G. P., Kastner, J., Li, J., Harnden, Jr., F. R., Wolk, S., Murray, S. S., Lada, C. J., Muench, A. A., McCaughrean, M. J., Meeus, G., Damiani, F., Micela, G., Sciortino, S., Bally, J., Hillenbrand, L. A., Herbst, W., Preibisch, T., & Feigelson, E. D. 2005, ApJS, 160, 319
- Gorenstein, P. 1975, ApJ, 198, 95
- Grady, C. A., Woodgate, B., Bruhweiler, F. C., Boggess, A., Plait, P., Lindler, D. J., Clampin, M., & Kalas, P. 1999, ApJ, 523, L151
- Grady, C. A., Woodgate, B., Torres, C. A. O., Henning, T., Apai, D., Rodmann, J., Wang, H., Stecklum, B., Linz, H., Williger, G. M., Brown, A., Wilkinson, E., Harper, G. M., Herczeg, G. J., Danks, A., Vieira, G. L., Malumuth, E., Collins, N. R., & Hill, R. S. 2004, ApJ, 608, 809
- Grady, C. A., Schneider, G., Hamaguchi, K., Sitko, M. L., Carpenter, W. J., Hines, D., Collins, K. A., Williger, G. M., Woodgate, B. E., Henning, T., Ménard, F., Wilner, D., Petre, R., Palunas, P., Quirrenbach, A., Nuth, III, J. A., Silverstone, M. D. & Kim, J. S. 2007, ApJ, 665, 1391
- Gregory, S. G., Jardine, M., Cameron, A. C. & Donati, J.-F. 2006, MNRAS, 373, 827
- Grevesse, N., & Sauval, A. J. 1998, Space Science Reviews, 85, 161
- Güdel, M., Briggs, K. R., Arzner, K., Audard, M., Bouvier, J., Feigelson, E. D., Franciosini, E., Glauser, A., Grosso, N., Micela, G., Monin, J.-L., Montmerle, T., Padgett, D. L., Palla, F., Pillitteri, I., Rebull, L., Scelsi, L., Silva, B., Skinner, S. L., Stelzer, B., & Telleschi, A. 2007, A&A, 468, 353

- Guimarães, M. M., Alencar, S. H. P., Corradi, W. J. B., & Vieira, S. L. A. 2006, *A&A*, 457, 581
- Günther, H. M., Liefke, C., Schmitt, J. H. M. M., Robrade, J., & Ness, J.-U. 2006, *A&A*, 459, L29
- Hamaguchi, K., Yamauchi, S., & Koyama, K. 2005, *ApJ*, 618, 360
- Herbig, G. H. 1960, *ApJS*, 4, 337
- Houck, J. C., & Denicola, L. A. 2000, in *ASP Conf. Ser. 216: Astronomical Data Analysis Software and Systems IX*, Vol. 9, 591
- Hu, J. Y., Blondel, P. F. C., The, P. S., Tjin A Djie, H. R. E., de Winter, D., Catala, C., & Talavera, A. 1991, *A&A*, 248, 150
- Hu, J. Y., The, P. S., & de Winter, D. 1989, *A&A*, 208, 213
- Hubrig, S., Pogodin, M. A., Yudin, R. V., Schöller, M., & Schnerr, R. S. 2007, *A&A*, 463, 1039
- Hubrig, S., Schöller, M., & Yudin, R. V. 2004, *A&A*, 428, L1
- Huenemoerder, D. P., Kastner, J. H., Testa, P., Schulz, N. S., & Weintraub, D. A. 2007, *ApJ*, 671, 000
- Huenemoerder, D. P., Testa, P., & Buzasi, D. L. 2006, *ApJ*, 650, 1119
- Ishibashi, K., Dewey, D., Huenemoerder, D. P., & Testa, P. 2006, *ApJ*, 644, L117
- Kastner, J. H., Huenemoerder, D. P., Schulz, N. S., Canizares, C. R., & Weintraub, D. A. 2002, *ApJ*, 567, 434
- Larson, R. B. 1972, *MNRAS*, 157, 121
- Luhman, K. L. 2004, *ApJ*, 616, 1033
- Maggio, A., Flaccomio, E., Favata, F., Micela, G., Sciortino, S., Feigelson, E. D. & Getman, K. V. 2007, *ApJ*, 660, 1462
- Malfait, K., Bogaert, E., & Waelkens, C. 1998, *A&A*, 331, 211
- Mannings, V., & Sargent, A. I. 1997, *ApJ*, 490, 792
- Muzerolle, J., D'Alessio, P., Calvet, N., & Hartmann, L. 2004, *ApJ*, 617, 406

- Ness, J.-U., Güdel, M., Schmitt, J. H. M. M., Audard, M., & Telleschi, A. 2004, *A&A*, 427, 667
- Palla, F., & Stahler, S. W. 1993, *ApJ*, 418, 414
- Perryman, M. A. C., Lindegren, L., Kovalevsky, J., Hoeg, E., Bastian, U., Bernacca, P. L., Crézé, M., Donati, F., Grenon, M., van Leeuwen, F., van der Marel, H., Mignard, F., Murray, C. A., Le Poole, R. S., Schrijver, H., Turon, C., Arenou, F., Froeschlé, M., & Petersen, C. S. 1997, *A&A*, 323, L49
- Preibisch, T., Kim, Y.-C., Favata, F., Feigelson, E. D., Flaccomio, E., Getman, K., Micela, G., Sciortino, S., Stassun, K., Stelzer, B., & Zinnecker, H. 2005, *ApJS*, 160, 401
- Sanz-Forcada, J., Brickhouse, N. S., & Dupree, A. K. 2003, *ApJS*, 145, 147
- Schmitt, J. H. M. M., Robrade, J., Ness, J.-U., Favata, F., & Stelzer, B. 2005, *A&A*, 432, L35
- Skinner, S. L., Güdel, M., Audard, M., & Smith, K. 2004, *ApJ*, 614, 221
- Skinner, S. L., & Yamauchi, S. 1996, *ApJ*, 471, 987
- Smith, R. K., Brickhouse, N. S., Liedahl, D. A., & Raymond, J. C. 2001, *ApJ*, 556, L91
- Stelzer, B., Micela, G., Hamaguchi, K., & Schmitt, J. H. M. M. 2006, *A&A*, 457, 223
- Stelzer, B., & Schmitt, J. H. M. M. 2004, *A&A*, 418, 687
- Swartz, D. A., Drake, J. J., Elsner, R. F., Ghosh, K. K., Grady, C. A., Wassell, E., Woodgate, B. E., & Kimble, R. A. 2005, *ApJ*, 628, 811
- Tatulli, E., Isella, A., Natta, A., Testi, L., Marconi, A., Malbet, F., Stee, P., Petrov, R. G., & et al. 2007, *A&A*, 464, 55
- Telleschi, A., Güdel, M., Briggs, K. R., Skinner, S. L., Audard, M., & Franciosini, E. 2007, *A&A*, 468, 541
- Telleschi, A., Güdel, M., Briggs, K. R., Audard, M., Ness, J. U., & Skinner, S. L. 2005, *ApJ*, 622, 653
- Testa, P., Drake, J., & Peres, G. 2004, *ApJ*, 617, 508
- Tout, C. A., & Pringle, J. E. 1995, *MNRAS*, 272, 528
- van den Ancker, M. E., de Winter, D., & Tjin A Djie, H. R. E. 1998, *A&A*, 330, 145

- Wade, G. A., Bagnulo, S., Drouin, D., Landstreet, J. D., & Monin, D. 2007, MNRAS, 376, 1145
- Wade, G. A., Drouin, D., Bagnulo, S., Landstreet, J. D., Mason, E., Silvester, J., Alecian, E., Böhm, T., Bouret, J.-C., Catala, C., & Donati, J.-F. 2005, A&A, 442, L31
- Walker, H. J., & Wolstencroft, R. D. 1988, PASP, 100, 1509
- Waters, L. B. F. M., & Waelkens, C. 1998, ARA&A, 36, 233
- Zinnecker, H., & Preibisch, T. 1994, A&A, 292, 152

Table 9. Velocity from Line Shifts Measurements

Ion	λ [Å]	v_{rad} [km s ⁻¹] ^a
Si XIV	6.183	0.0 [−140, +240]
Mg XII	8.422	76 [−61, +220]
Mg XI	9.169	120 [−100, +220]
Ne X	12.135	0.0 [−96, +85]
Fe XVII	15.014	43 [−52, +100]
Fe XVII	17.096	41 [−37, +110]
O VIII	18.970	43 [−31, +130]

^aThe 99% confidence intervals are listed in square brackets.